Journal of Wind Engineering & Industrial Aerodynamics 227 (2022) 105078

Contents lists available at ScienceDirect

Journal of Wind Engineering & Industrial Aerodynamics

journal homepage: www.elsevier.com/locate/jweia

Evaporating waterbody effects in a simplified urban neighbourhood: A RANS analysis

Petros Ampatzidis [a,*], Carlo Cintolesi [b], Andrea Petronio [c], Silvana Di Sabatino [b], Tristan Kershaw [a]

[a] Department of Architecture and Civil Engineering, University of Bath, Claverton Down, BA2 7AY, Bath, UK
[b] Department of Physics and Astronomy, University of Bologna, via Irnerio 46, 40126, Bologna, Italy
[c] IEFLUIDS s.r.l., Piazzale Europa 1, 34127, Trieste, Italy

ARTICLE INFO

Keywords:
Urban waterbody
Blue space
Nature-based solutions
Evaporation
CFD
RANS
OpenFOAM

ABSTRACT

The incorporation of nature-based solutions comprising green and blue infrastructure is often touted as a way to cool cities and enhance pollutant removal. However, there is little agreement between different methodologies to measure the effect of any single intervention. Here, we present 3D steady RANS simulations to investigate the influence of waterbody on in-canyon flow structure, temperature (T^*) and water vapour (ω^*) distribution in a simplified urban neighbourhood. A novel solver that captures evaporation effects is developed and validated against wind tunnel experiments. Simulations are performed under neutral atmospheric conditions for forced- and mixed-convection cases and different air–water temperature differences, indicative of either daytime or night-time conditions. Results under forced convection show minimal impact on the flow structure, whilst T^* and ω^* effects are distributed primarily over and around the water surface. However, the mixed-convection case shows that a cooler waterbody weakens the principal vortex in the open square, whilst T^* and ω^* effects reach further upwind and are more widely distributed in the spanwise direction. A warmer waterbody is shown to disrupt the skimming flow structure, indicating a possible heat and pollutant removal mechanism from around the waterbody and also downwind canyons.

1. Introduction

The combined effect of climate change and future urban growth will further increase air temperatures within cities, contributing more to what is known as urban overheating (IPCC, 2021; Santamouris, 2015). Furthermore, more frequent heatwaves compounded by hotter days and warmer nights will increase the risk of heat stress in cities, exacerbating the effects of the Urban Heat Island (UHI) phenomenon on public health (Arias et al., 2021; Liu et al., 2017). In addition, the isolation of the urban microclimate from the atmosphere above concentrates air pollution at street level in poorly ventilated cities, posing another major health threat (Vardoulakis et al., 2003). It is, therefore, of paramount importance for policymakers and city planners to find ways to regulate the thermal urban environment, improve airflow circulation and ventilation to enhance pollutant removal and create a sustainable and healthy space for today's and future citizens (Di Sabatino et al., 2020; Ibrahim et al., 2021).

There is a growing awareness that Nature-Based Solutions (NBS) – actions inspired by, supported by or copied from nature (EC, 2015) – can contribute to climate change mitigation and adaptation within cities (Gallotti et al., 2021; Seddon et al., 2020). Yet, the evidence-based integration of NBS into climate and development policies calls for further research for quantifying their effectiveness compared to technology-based solutions (Kabisch et al., 2016; Ruangpan et al., 2020; Seddon et al., 2020).

A relevant action that falls under the umbrella concept of NBS is the incorporation of green and blue infrastructure networks in cities. Ranging from urban parks, green roofs and street vegetation to urban ponds, wetlands and irrigation systems, the implementation of green and blue spaces has long been considered a possible mitigation strategy to ameliorate the adverse effects of the UHI (Arnfield, 2003; Gunawardena et al., 2017; Santamouris and Osmond, 2020). Moreover, their ability to alter the aerodynamic properties of the cityscape, increase evapotranspiration and, thus, promote vertical transport of heat, air and pollutants have placed blue and green solutions high up in the climate change resilience agenda. Nonetheless, although green spaces have been studied to a reasonable extent, less attention has been paid to blue spaces' thermal behaviour and overall contribution (Ampatzidis and Kershaw, 2020; Bartesaghi Koc et al., 2018; Gunawardena et al., 2017).

To date, there has been little agreement on how and whether blue spaces relieve heat stress under hot weather conditions. On the one

* Corresponding author.
E-mail address: p.ampatzidis@bath.ac.uk (P. Ampatzidis).

https://doi.org/10.1016/j.jweia.2022.105078
Received 8 March 2022; Received in revised form 28 June 2022; Accepted 28 June 2022
Available online 6 July 2022

hand, blue spaces are known to provide cooling by evaporation and sensible heat transfer due to air–water temperature gradients (Tominaga et al., 2015). Several researchers have reported a nocturnal warming effect when the water can be warmer than the air due to its high thermal capacity (Heusinkveld et al., 2014; Steeneveld et al., 2014; Theeuwes et al., 2013; Žuvela-Aloise et al., 2016). On the other hand, there is no consensus among the existing literature regarding the magnitude of any cooling or warming and the influencing factors (Jacobs et al., 2020; Klok et al., 2019; Yu et al., 2020).

The lack of consensus is also portrayed in the different results reported by various methods. Remote sensing techniques, which comprise most of the existing research focusing on blue spaces, tend to overestimate the cooling potential (values ranging 1–10 °C) (Ampatzidis and Kershaw, 2020; Jacobs et al., 2020). Although the use of satellite images can lead to informative qualitative conclusions regarding the overall performance of blue spaces (Sun and Chen, 2012; Xue et al., 2019), it does not account for the latent heat of vaporisation and primarily concerns studies of a particular instant in time. On the other hand, numerical studies employing Computational Fluid Dynamics (CFD) or three-dimensional microclimate models, like ENVI-met, lack a consistent approach as they usually evaluate blue spaces under different background climatic conditions, urban form and model parameters (Ampatzidis and Kershaw, 2020). Additionally, it is common to encounter studies involving both green and blue spaces, which makes it difficult to assess the contribution of each solution. This also applies to field measurements whose documented blue space cooling effects range from 3-4 °C (Huang et al., 2008; Ishii et al., 1991) to around 1 °C (Heusinkveld et al., 2014; Klok et al., 2019; Saaroni and Ziv, 2003). However, these discrepancies can be attributable to different climatic conditions, surrounding urban form and the synergistic effect of blue and green spaces.

The evidence presented so far suggests the need to study the influence of selected factors on the overall performance of blue space, independent of the background climate. Numerical modelling is a tool that offers the ability to isolate different parameters and assess their impact against a baseline model. However, until recently, only few studies have isolated various influencing factors to determine the performance of blue spaces more carefully. Notably, Theeuwes et al. (2013) have assessed the thermal effects of waterbodies in an idealised city based on their spatial distribution, size and surface temperature. This lack of controlled studies, combined with their limited number compared to other UHI mitigation strategies, calls for further research on this area.

Urban planning has its most significant impact on the urban canopy layer (UCL), i.e. the atmospheric layer extending from ground to roof level, where both pollutants – along with their sources – and humans coexist. One of the main mechanisms of diluting pollutants within the UCL is the enhancement of ventilation and promoting mitigation techniques that induce vertical mixing. Numerous studies have assessed the effect of a wide range of features on pollutant dispersion, namely the spacing between buildings, roof shape, street aspect ratio, building packing density and wind direction (Buccolieri et al., 2015; Cintolesi et al., 2021; Di Sabatino et al., 2013; Trindade da Silva et al., 2021). However, identifying mitigation strategies that can simultaneously promote pollutant dilution and improvement of thermal comfort is currently a primary concern (Di Sabatino et al., 2020). In this context, green spaces have been considered a possible removal mechanism given that they are carefully positioned so that they do not create a canopy and consequent trapping of pollutants (Abhijith et al., 2017; McMullan and Angelino, 2022). The addition of water vapour in the atmosphere can also induce vertical motion as water vapour is less dense than air. However, far too little attention has been paid to how this applies to blue spaces in an urban environment. During the day, the UHI can promote vertical mixing as urban surfaces get warmer. But during the night, when most cities experience a near-neutral or stable atmosphere, vertical mixing is compressed, and thus the nocturnal impact of blue space may be substantial.

In light of the above, this study aims to address the influence of blue space on the airflow, temperature and water vapour concentration fields within a uniform 7 × 3 building array under neutral atmospheric stability. The central building is removed and replaced with a waterbody, resembling an open square configuration. A baseline isothermal case without the waterbody is compared against cases under forced and mixed convection. The influencing parameter is the reference wind speed at roof level, which leads to different convection regimes. A case with a cooler and warmer waterbody for each convection regime is considered. The reference temperature difference between the water surface and the surrounding air is constant at $\Delta T_0 = \pm 2$ °C. Modelling of evaporation is achieved through the adaptation and modification of an in-house solver developed gradually by Petronio (2010), Sosnowski (2013) and Cintolesi (2016) within the Doctoral School of Environmental and Industrial Fluid Mechanics of the University of Trieste.

This paper is structured as follows: Section 2 provides an overview of the numerical model applied to this study. Section 3 presents the validation test cases, while Section 4 describes the simulation set-up and gives an overview of the simulation scenarios. In Section 5, the computational results, with and without the waterbody, are shown, along with a discussion on the implications of the problem. Finally, in Section 6, conclusions are drawn.

2. Simulation approach

2.1. Governing equations

The ambient fluid is composed of air and water vapour, considered as a mixture of ideal gases and modelled as an incompressible and viscous Newtonian fluid. The buoyancy force, induced by temperature (T [K]) and vapour concentration (ω [–]) gradients, is introduced via the Boussinesq approximation, which is considered suitable for the present case as it leads to errors of the order of 1% for temperature variations of $\Delta T = 15$ K for air and $\Delta T = 2$ K for water (Ferziger and Perić, 2002). The equations describing the flow read:

$$\frac{\partial u_j}{\partial x_j} = 0, \tag{1}$$

$$\frac{\partial u_j u_i}{\partial x_j} = -\frac{1}{\rho_0}\frac{\partial p}{\partial x_i} + \nu\frac{\partial^2 u_i}{\partial x_j x_j} + b_i, \tag{2}$$

$$b_i = g_i\left(1 - \beta_T \Delta T - \beta_\omega \Delta\omega\right), \tag{3}$$

where u_i is the velocity component in the x_i direction [m s^{-1}], p is pressure [Pa], ρ_0 is the reference fluid density [kg m^{-3}], ν is the molecular kinematic viscosity [m^{2}s^{-1}], b_i is the buoyancy force [m s^{-2}], g_i is the gravitational acceleration [m s^{-2}].

The buoyancy force is expressed in terms of variation of temperature ΔT and vapour concentration $\Delta\omega$ with respect to reference values and their volume expansion coefficients β_T [K^{-1}] and β_ω [–]. The equations for temperature and vapour concentration read:

$$\frac{\partial}{\partial x_j}\left(T u_i\right) - \alpha_T\frac{\partial^2 T}{\partial x_k \partial x_k} = S_e, \tag{4}$$

$$\frac{\partial}{\partial x_j}\left(\omega u_i\right) - \alpha_\omega\frac{\partial^2 \omega}{\partial x_k \partial x_k} = 0, \tag{5}$$

where α_T and α_ω are the molecular and turbulent diffusivities of air and water vapour, respectively, and S_e is the evaporation heat sink term.

The influence of solar radiation is neglected as this study attempts an initial assessment of evaporation effects within an urban environment with the lowest possible complexity.

2.2. Evaporation model

The simulation of the complex thermo-fluid dynamics of an evaporating waterbody is a challenging issue that requires, amongst other things, to accurate reproduce the internal motions of water and the heat exchange at the air–water interface (Cintolesi et al., 2016). The present study focuses on the impact of water evaporation on the air circulation in an urban neighbourhood and, as a first approximation, the complete simulation of water dynamics is not taken into account. Hence, the waterbody is considered at rest (no internal motion) and isothermal. Under these hypotheses, the water medium is not directly solved but rather modelled through the thin-film assumption, i.e. the waterbody is modelled as a wet surface that can evaporate infinitely (Petronio, 2010).

The evaporation velocity u_ω is estimated with a semi-impermeable model (Welty et al., 2007) and essentially depends on the vapour gradient in the surface normal direction. It reads:

$$u_{\omega,i} = -\frac{\alpha_\omega}{1-\omega_\Gamma}\left(\frac{d\omega}{dn_i}\bigg|_\Gamma\right) n_i, \tag{6}$$

where the subscript Γ indicates that the quantities are evaluated at the air–water interface and n_i is the vector normal to the interface pointing to the inner side of the domain. The vapour concentration at the interface is computed as in Cintolesi et al. (2016), by the following empirical formula:

$$\omega_\Gamma = \frac{M_v}{M_a}\,\frac{\phi_\Gamma\; p_{sat}(T_\Gamma)}{p-\left(1-\frac{M_v}{M_a}\right)\phi_\Gamma\; p_{sat}(T_\Gamma)}, \tag{7}$$

where $M_a = 28.97$ g/mol and $M_v = 18.02$ g/mol are the molar masses of air and water vapour, respectively, ϕ_Γ is the relative humidity, and p_{sat} is the saturation pressure at the interface. Relative humidity at the interface is $\phi_\Gamma = 1$, as the air–water interface is assumed to be at saturation conditions. The saturation pressure p_{sat} at the interface is evaluated based on the interface temperature using Buck's formula:

$$p_{sat}(T) = 611.85\exp\left(\frac{17.502(T-273.15)}{240.9+(T+273.15)}\right). \tag{8}$$

The energy subtracted from the system due to evaporation is modelled via the heat sink term S_e in Eq. (4). It is applied numerically to the first cells adjacent to the water surface, whilst it is zero everywhere else. It is modelled as:

$$S_e = -\frac{\rho^* L_h}{\rho C_p}\frac{\partial u_{\omega_i}}{\partial x_i}, \tag{9}$$

where $\rho^* = 1.184$ kg/m^3 is the density of the mixture of air and water vapour (considered equal to the density of the air with reasonable accuracy, see Çengel and Ghajar, 2015), $L_h = 2.45\times10^6$ J/kg is the latent heat of vaporisation, and $\rho C_p = 1192$ J/m K is the volumetric heat capacity.

Notice that the present model can simulate both evaporation and condensation. However, only the cooling effect of evaporation is taken into account, whereas the warming effect of condensation on the water surface is neglected as water is assumed isothermal. Additional information and details of the model can be found in Petronio (2010), Sosnowski et al. (2013) and Cintolesi et al. (2016, 2017).

2.3. Numerical approach and turbulence modelling

The simulations adopt the Reynolds-Averaged Navier–Stokes (RANS) approach for turbulent flows. The averaging in time of Eq. (2) introduces the Reynolds stress $\tau_{ij} = \langle u_i' u_j' \rangle$, where u_i' is the velocity fluctuation from the mean, and the angular brackets denote the time average. The anisotropic part τ_{ij}^a is then modelled using the eddy-viscosity hypothesis:

$$\tau_{ij}^a = -2\nu_t\langle S_{ij}\rangle, \tag{10}$$

where ν_t is the turbulent viscosity to be determined and $S_{ij} = 0.5(\partial u_i/\partial x_j + \partial u_j/\partial x_i)$ is the strain-rate tensor. See Pope (2013) for details.

The standard $k-\varepsilon$ model and two other derived models are used to close the system, giving an explicit expression for ν_t. Those models are: the $k-\varepsilon$ model as initially proposed by Launder and Spalding (1974); the renormalisation group (RNG) model described by Yakhot and Orszag (1986); the Realizable $k-\varepsilon$ model introduced by Shih et al. (1995). The performance of the three models is investigated in the validation section and the best performing model is selected for the reproduction of the case study. As they are well-known turbulence models that have been widely employed for simulations for several decades, for the sake of conciseness, their formulation is not reported here. Instead, the authors refer to the original papers for their description.

By analogy with the momentum equation, the averaging in time for Eqs. (4) and (5) for temperature and vapour concentration, respectively, leads to the appearance of turbulent flux terms, i.e. $h_i = \langle u_i' T' \rangle$ and $\ell_i = \langle u_i' \omega' \rangle$, respectively. They are modelled through the gradient hypothesis as $h_i = -\alpha_{T,t}\;\partial T/\partial x_i$ and $\ell_i = -\alpha_{\omega,t}\;\partial\omega/\partial x_i$, where the turbulent diffusivity of temperature and vapour are modelled by using the turbulent Prandtl (Pr_t) and Schmidt (Sc_t) numbers, i.e. $\alpha_{T,t} = \nu_t/Pr_t$ and $\alpha_{\omega,t} = \nu_t/Sc_t$, respectively.

In order not to directly resolve the wall-boundary layer, wall functions are used for active scalars. For temperature, $\alpha_{T,t}$ is computed assuming a logarithmic distribution of the potential temperature in the first cell. For vapour, there is not a similar wall function for $\alpha_{\omega,t}$. The relative magnitude of heat and mass diffusion in the thermal and concentration boundary layers is expressed with the dimensionless Lewis number $Le = a/D$, where a and D are the thermal and mass diffusivities, respectively. A value of $Le^{3/2}$ close to unity assures a heat and mass transfer analogy, which holds in this study as $Le = 0.9$. In general, cases involving the evaporation of water vapour into the air can use the heat–mass analogy with confidence (Çengel and Ghajar, 2015). Therefore, a new wall function for $\alpha_{\omega,t}$ is introduced based on the respective function for $\alpha_{T,t}$ by using the Schmidt number as the scaling variable. The performance of the new wall function is investigated in Section 3.2.

2.4. Algorithm and numerical schemes

The numerical simulations are carried out using the open-source software OpenFOAM (ESI-OpenCFD, 2006) for computational fluid dynamics. The authors have developed an in-house solver to implement the evaporation/condensation model presented in Section 2.2. The new solver is based on the steady-state solver *buoyantBoussinesqSimpleFoam* for buoyant, turbulent flow of incompressible fluids provided in OpenFOAM. Notably, the main algorithm is modified to introduce the vapour concentration, while new boundary conditions have been developed to account for the sink term in Eq. (9) and the water evaporation/condensation. The authors refer to the OpenFOAM documentation (ESI-OpenCFD, 2006) for the turbulence model implementation.

The solution algorithm is the Semi-Implicit Method for Pressure Linked Equations (SIMPLE) (Patankar, 1980; Patankar and Spalding, 1972). All discretisation schemes are second-order accurate: central difference schemes are used for velocity, temperature and vapour concentration, whilst a stabilised version of such scheme that uses the Sweby limiter (Sweby, 1984) is used for turbulent kinetic energy (TKE) k and its dissipation rate ε. Convergence was ensured based on the residuals and by monitoring the change of velocity values at specific points within the building array.

2.5. Dimensionless parameters

The flow regimes for the problem under consideration are characterised by the Reynolds number based on the upstream reference velocity U_0 and the building width L, that reads:

$$Re = \frac{U_0 L}{\nu} \tag{11}$$

and represents the ratio between inertial and viscous forces. Natural convection regimes are described by the Grashof number, which represents the ratio of buoyant to viscous forces:

$$Gr = \frac{gL^3}{\nu^2}\left(\beta_T \Delta T_0 + \beta_\omega \Delta\omega_0\right), \tag{12}$$

where $\Delta T_0 = |T_w - T_a|$ ($\Delta\omega_0 = |\omega_w - \omega_a|$) is the reference difference of temperature (vapour concentration), with T_a (ω_a) the inflow air temperature (vapour concentration) and T_w (ω_w) the waterbody temperature (vapour concentration). Hence, the buoyant forces include the contribution of both temperature and vapour concentration gradients.

The relative importance of the inertial and convective motions is indicated by the Richardson number $Ri = Gr/Re^2$, which is the ratio of the buoyant to the flow shear term: if $Ri \gg 1$, natural convection dominates the flow; if $Ri \ll 1$, forced convection drives the overall flow. According to Pauken (1998), who conducted measurements of evaporation rates over a large-diameter evaporation pan, values of $0.1 < Ri < 5$ can be considered a mixed-convection flow regime. For writing convenience, the Richardson number is defined with a positive or negative sign to indicate when the waterbody is warmer or cooler than the surrounding atmosphere, i.e. $Ri = +|Ri|$ if $\Delta T_0 > 0$, while $Ri = -|Ri|$ otherwise.

In the literature, the appropriate definition of the Richardson number has been subject to considerable debate. As Zhao et al. (2020) have recently pointed out, researchers tend to derive Ri in different ways, i.e. using temperature differences between the air at roof and ground level, upwind and downwind walls, or heated surfaces and ambient air. Other studies have employed a local Richardson number (Allegrini et al., 2012; Fernando et al., 2010), where temperature and velocity close to the surface of interest are taken as the reference value. It is worth mentioning though, that in case of a flow subject to an isothermal urban canyon, the definition of Ri is more straightforward. Hence, as the building and ground surfaces of this study are in thermal equilibrium with the ambient air, the definition of Ri described above has considered characteristic of the flow regime.

Unless otherwise specified, quantities are made non-dimensional utilising the building height H for length, the free-stream velocity U_0 for velocity. Temperature is normalised as $T^* = (T - T_a)/\Delta T_0$ and vapour concentration as $\omega^* = (\omega - \omega_a)/\Delta\omega_0$ in the following.

2.6. Validation metrics

Validation metrics proposed by the European COST Action 732 (Schatzmann et al., 2010) are used to appraise the accuracy of the simulations compared to the experimental datasets. If P_i and O_i are the simulation and observed values, respectively, for $i = 1, \ldots, N$ where N is the total number of measurement points; the hit rate q and the fraction of the prediction within a factor two of observations ($FAC2$) are defined as:

$$q = \frac{1}{N}\sum_{i=1}^{N} n_i \quad \text{with} \quad n_i = \begin{cases} 1, & \text{if } \left|\frac{P_i - O_i}{P_i}\right| \le D_q \text{ or } |P_i - O_i| \le W_q \\ 0, & \text{otherwise} \end{cases} \tag{13}$$

$$FAC2 = \frac{1}{N}\sum_{i=1}^{N} n_i \quad \text{with} \quad n_i = \begin{cases} 1, & \text{if } 0.5 \le P_i/O_i \le 2 \\ 0, & \text{otherwise} \end{cases} \tag{14}$$

where the threshold parameters are $D_q = 0.25$ and $W_q = 0.03$ for velocity, and $D_q = 0.25$ and $W_q = 0.003$ for TKE (Gousseau et al., 2013; Tominaga, 2015). Both metrics take values in $[0, 1]$, with value 1 indicating a perfect match between simulation and reference dataset. Hereafter, the threshold values of $q \ge 0.66$ and $FAC2 \ge 0.5$ are taken as indicators of a satisfactory validation (Schatzmann et al., 2010; Toja-Silva et al., 2015).

Additional metrics are the normalised mean square error ($NMSE$) and the fractional bias (FB) that both reveal systemic errors, calculated as:

$$NMSE = \frac{\langle (O - P)^2 \rangle_N}{\langle O \rangle_N \langle P \rangle_N}, \quad \text{and} \quad FB = 2\frac{\langle O \rangle_N - \langle P \rangle_N}{\langle O \rangle_N + \langle P \rangle_N}, \tag{15}$$

where angular brackets $\langle \cdot \rangle_N$ denote the average over the total number of data points. The ideal value for FB and $NMSE$ is zero, while $|FB| < 0.3$ and $NMSE < 4$ indicates a successful validation (Schatzmann et al., 2010; Toja-Silva et al., 2015).

3. Validation

To the best of the authors' knowledge, a validation case considering the interaction between turbulent airflow, natural convection and water's change of phase in an urban context is not present in the literature. Hence, the validation of the simulation approach is performed against three benchmark cases: (i) the turbulent airflow around a single building, Section 3.1; (ii) the evaporation from an open water surface, Section 3.2; (iii) the turbulent airflow past a building array, which can be found in Appendix. Three simulations utilising three different turbulence models ($k - \varepsilon$, RNG, Realizable) have been performed and compared (see Section 2.3).

3.1. Single building

Case A of the wind tunnel experiments conducted by Architectural Institute of Japan (2016) (hereafter *AIJ2016*) is numerically reproduced; it consists of a single rectangular building placed on a flat surface impacted by turbulent airflow. Detailed measurements were reported by Meng and Hibi (1998) and subsequently used in various numerical studies for validation purposes (Mochida et al., 2002; Tominaga et al., 2004; Yoshie et al., 2007). A short description of the case set-up is presented here, while further details can be found in the referenced articles.

The building height is $2b = 0.16$ m, while the width and length is $b = 0.08$ m. The reference velocity at the building top is $U_0 = 4.491$ m/s, which leads to a Reynolds number of $Re = 2.4 \times 10^4$. The domain size is $21.5b \times 13.75b \times 11.25b$ and is discretised with $84 \times 82 \times 40$ cells in the streamwise (x), spanwise (y) and vertical (z) dimension, respectively. The ground is a flat surface with an aerodynamic roughness length equal to $z_0 = 1.8 \times 10^{-4}$. The flow is driven by inlet condition: interpolated profiles of velocity $u(z)$ and TKE were imposed according to the experimental profiles. The TKE dissipation rate ε is estimated assuming local equilibrium between the production and dissipation of TKE ($P_k = \varepsilon$).

Fig. 1 shows the streamwise velocity U and TKE profiles along several vertical lines at the centre plane $y/b = 0$ and at different locations in the x-direction. Simulation results (lines) are compared against experimental measurements (symbols) with the dotted lines representing the reference axis of each vertical line. In general, simulations agree well with the experimental data. In Fig. 1a, the simulated velocity profiles exhibit some differences in the above-roof area of the building ($2 \le z/b \le 2.5$), where the RNG is slightly more accurate than the $k - \varepsilon$ and Realizable models. Discrepancies are also detected in the behind-building area ($0.75 \le x/b \le 2$ and $0 \le z/b \le 2$), where all the simulations slightly underestimate reference values and predict a larger recirculation region: at $x/b = 2$, the experimental value of U is positive, whereas all three turbulence models predict negative values near the ground ($z/b < 1$). This is due to the known incapability of steady-state RANS models to reproduce vortex shedding in the wake of buildings (Blocken, 2014; Shirzadi et al., 2017). Vertical velocities are also scrutinised at the same vertical lines. All simulated profiles practically collapse to the experimental data and, thus, they are not shown. In Fig. 1b, all simulations overestimate TKE close to the upwind side of the building and upwind corners of the roof ($-0.75 \le x/b \le -0.25$), which agrees with the simulations conducted by *AIJ2016* and the existing literature (Toja-Silva et al., 2018). However, the RNG model predicts values closer to the experimental data than the standard $k-\epsilon$ and Realizable models. The models behave the same in the above-roof area ($2 \le z/b \le 2.5$), presenting expected discrepancies with the

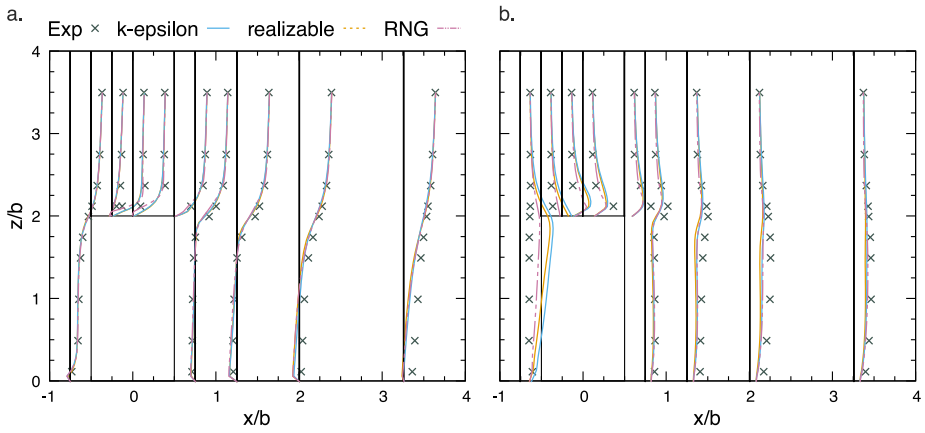

Fig. 1. Streamwise velocity component U (a) and TKE (b) along nine selected vertical lines (black dashed lines) at several locations in x-direction and at the centre plane $y/b = 0$. Data from: Exp, experimental data from AIJ2016; k-epsilon, simulation with $k-\varepsilon$ turbulent model; Realizable, simulation with $k-\varepsilon$ realizable model; RNG, simulation with renormalisation group model.

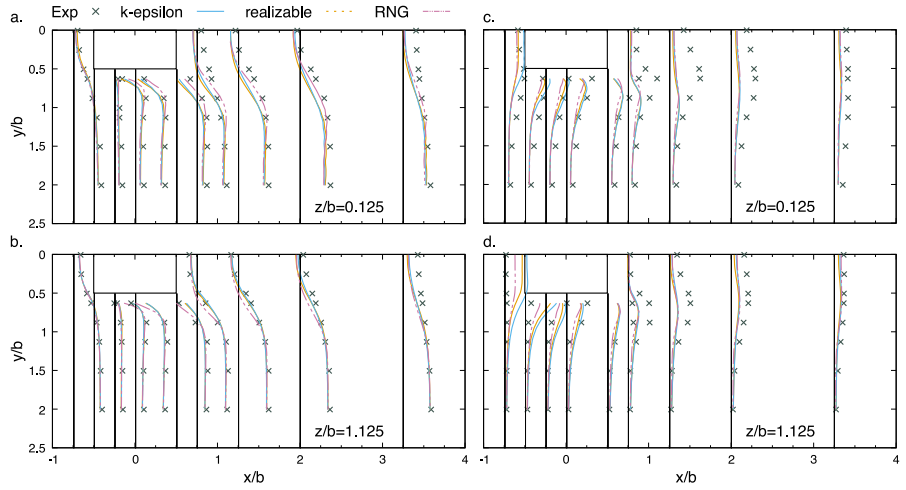

Fig. 2. Streamwise velocity U (panels a, b) and TKE k (panels c, d) at two horizontal planes and two selected heights: close to the ground at $z/b = 0.125$, and near the building mid-high at $z/b = 1.125$. Profiles along horizontal lines (dashed black lines) at several locations in x-direction. Comparison between simulations and experimental data as in Fig. 1.

reference values due to the excessive turbulent diffusion. In the behind-building area ($0.75 \leq x/b \leq 2$ and $0 \leq z/b \leq 2$), a general agreement with the experiment is evident for all models, with more significant discrepancies present farther from the building edge.

Fig. 2 shows the profiles of U and TKE on the horizontal plane at different heights, namely $z/b = 0.125$ and $z/b = 1.125$. In Fig. 2a, b, the selected turbulence models correctly reproduce the U profiles except for underestimating values in the building's wake region ($0.75 \leq x/b \leq 2$), especially in the plane near the ground ($z/b = 0.125$). Again, close to the building edges, the RNG model shows the lowest discrepancies compared to the $k-\varepsilon$ and Realizable models. As it can be seen in Fig. 2c, TKE profiles closer to the ground ($z/b = 0.125$) are captured well by the three models upwind ($-0.75 \leq x/b \leq -0.25$), whereas there is an underestimation of TKE values in the wake of the building ($0.75 \leq x/b \leq 2$). However, farther from the ground (Fig. 2d), at $z/b = 1.125$, TKE values are overestimated upwind with the RNG predicting values closer to the experimental ones, whilst all three models underestimate TKE in the wake region, albeit with lower discrepancies compared to the profiles at $z/b = 0.125$.

Fig. 3 reports the linear regression conducted for U (top panels) and TKE (bottom panels) against the experimental datasets. It concerns the total number of measurement points in the experiment and the respective probes in the simulations. The closer the estimated regression line (red line) is to the diagonal (black line), the better the agreement between simulated and experimental values. The performance of the models is also appraised with the coefficient of determination R^2. Overall, streamwise velocities from the three models agree well with the experiments, with the RNG model having a slightly larger value of the coefficient of determination ($R^2 = 0.93$). Notably, all models perform well within the high-velocity regions ($U/U_0 > 0.75$), whereas there are discrepancies in the low-velocity areas ($U/U_0 < 0.25$), where simulations underestimate streamwise velocities. This is in agreement with the results shown in Fig. 1. On the contrary, the general agreement of the TKE is poor and all the simulations mainly underestimate reference values. The coefficients of determination are very small, with the RNG model presenting a significantly larger value ($R^2 = 0.28$) compared to the other models. Additionally, the RNG model shows more minor differences where TKE values are overestimated ($-0.75 \leq x/b \leq -0.25$). This is in agreement with the profiles over the sampling lines presented in Figs. 1 and 2.

Table 1 presents the validation metrics described in Section 2.6 for U and TKE for the three simulations under consideration. All simulations exhibit similar values of q and $FAC2$, above the thresholds; hence, the velocity field is satisfactorily reproduced. In contrast, the metrics for TKE show some expected differences: q values are all below the threshold, whilst values of $FAC2$, $NMSE$ and FB satisfy their respective thresholds. RNG displays slightly better metrics, except for the FB.

Overall, the simulations can reproduce the general features of the flow despite the discrepancies arising in the reproduction of TKE.

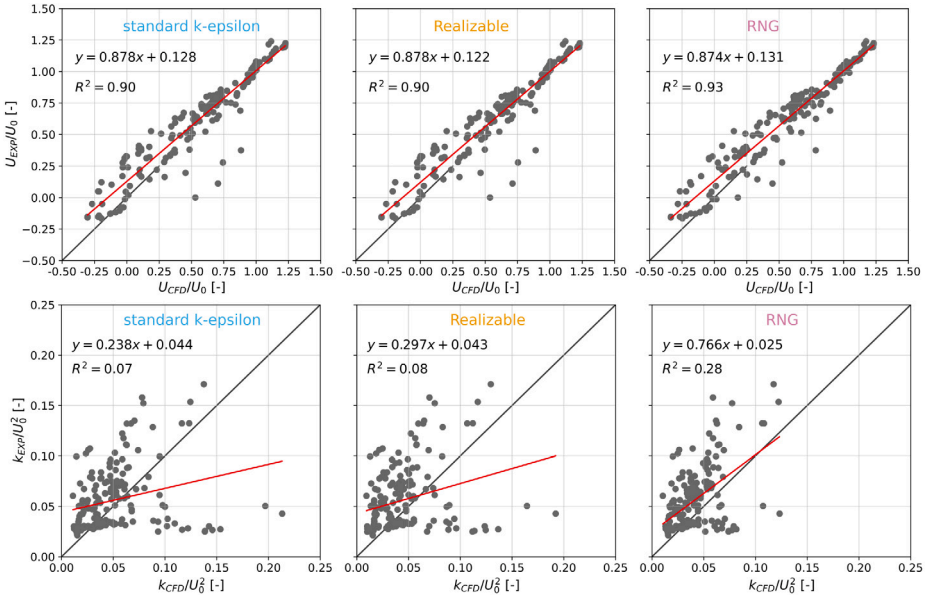

Fig. 3. Linear regression between simulated and experimental values of streamwise velocity ratio (U/U_0) and normalised turbulent kinetic energy (k/U_0^2), along with the values of coefficient of determination R^2.

Table 1
Validation metrics calculated for the streamwise velocity U and TKE, along with the relative thresholds (see Section 2.6).

Thresholds	U		TKE			
	q	$FAC2$	q	$FAC2$	$NMSE$	FB
	≥ 0.66	≥ 0.5	≥ 0.66	≥ 0.5	≤ 4	≤ 0.3
$k-\varepsilon$	0.70	0.83	0.29	0.70	0.57	0.13
Realizable	0.71	0.83	0.28	0.63	0.58	0.26
RNG	0.68	0.83	0.32	0.74	0.41	0.32

Furthermore, between the turbulence models used, the RNG shows a slightly better performance, which is consistent with the findings of Tominaga (2015).

3.2. Evaporation from a small-scale water surface

The validation of the evaporation model is carried out against experimental results from a wind tunnel study conducted by Kato et al. (2009). The case study consists of an evaporating plane water surface surrounded by air, and the measurements of air temperature and specific humidity are taken and discussed. The geometry, inflow profiles and thermophysical parameters, as well as the actual experimental output used to set-up the present simulations, were taken from Tominaga et al. (2015). The dimensions of the computational domain are those of the wind tunnel, i.e. $3.0 \times 1.0 \times 0.98$ m respectively in the streamwise, spanwise and vertical direction (or the x-, y- and z-direction). The domain discretisation consists of 60 × 20 × 50 cells following the one proposed by Tominaga et al. (2015). A turbulent Prandtl number $Pr_t = 0.85$ and a turbulent Schmidt number $Sc_t = 0.7$ are assumed. Constant values for air temperature, specific humidity and wind speed, respectively equal to $T_a = 20$ °C, $\omega_a = 0.008$ and $U_0 = 3$ m/s, are used at the inflow variables at a reference height of $H = 0.3$ m. The water depth is $d = 2$ cm, its surface temperature is $T_w = 16$ °C, and the aerodynamic roughness length is estimated at $z_0 = 2.6 \times 10^{-4}$ m. The Reynolds number based on the reference velocity and height is $Re = 6 \times 10^4$.

Fig. 4 shows the dimensionless temperature and vapour concentration profiles along three horizontal lines close to the water surface at height $z_1/H = 0.13$, $z_2/H = 0.07$, $z_1/H = 0.017$ and along the streamwise direction. Quantities are made non-dimensional by the air temperature T_{Ref} and vapour concentration ω_{Ref} at height H above ground level. The three models accurately capture the pattern of air temperature decreasing with a decreasing rate, presenting negligible differences in their results (Fig. 4a). Closer to the water surface, at $z/H = 0.017$, the agreement with the reference values is evident. In contrast, more significant discrepancies are observed farther from the ground at $z/H = 0.07$ and $z/H = 0.13$, where simulations tend to underestimate air temperatures. Fig. 4b shows that the simulations reproduce similar profiles of vapour concentration distribution across the domain compared to the experimental values. Larger discrepancies are present closer to the water surface, at $z/H = 0.017$ and $z/H = 0.07$, whilst farther from it, at $z/H = 0.13$, there is a good agreement with the reference values. The differences in the results closer to the ground are, presumably, due to the introduction of the new wall function for $\alpha_{\omega,t}$ (see Section 2.3) or the inherent errors in the experimental data, as big jumps in vapour concentration values are observed at $z/H = 0.017$ and $z/H = 0.07$.

Overall, the validation shows that the three turbulence models reproduce the experiments satisfactorily, albeit with some differences. The RNG model performs better in the single building case, primarily because of the more accurate prediction of TKE, compared to the standard $k-\varepsilon$ and Realizable models. All models predict similar results when evaporation and temperature distribution is concerned. The validation of the building array case in Appendix demonstrates similar results for all turbulence models. Considering the above, the RNG model is selected for the simulations of this study. However, caution must be applied, as these findings are not, potentially, transferable to other urban configurations or when different experiments are employed.

4. Case study description

4.1. Problem definition and simulation outline

The effects on airflow, temperature and water vapour distribution of a waterbody in a city fabric are investigated with a simplified geometry, consisting of an idealised urban neighbourhood composed of 20 buildings arranged in a 7 × 3 grid. The central building has been removed and replaced by a square isothermal waterbody, as sketched in Fig. 5, creating an open square. Note that the waterbody is modelled as an evaporating surface with constant temperature and no depth, as

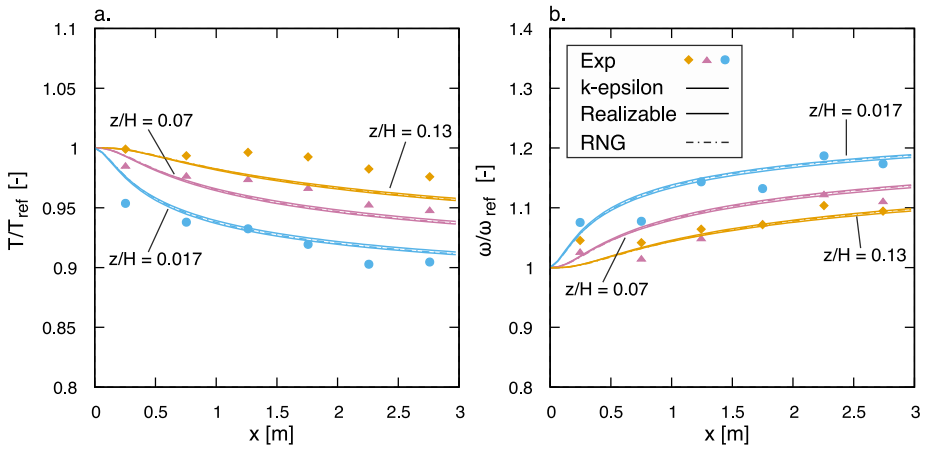

Fig. 4. Simulated normalised air temperature T/T_{Ref} (panel a) and normalised vapour concentration ω/ω_{Ref} (panel b) against experimental measurements along three sampling lines at different heights above the water surface.

Table 2
Configuration settings for the six simulations under consideration: characteristic airflow velocity (U_0), air–water temperature difference (ΔT_0) and dimensionless parameters.

Airflow	Mixed convection			Forced convection		
Water	Baseline	Warm	Cool	Baseline	Warm	Cool
U_0 [m/s]	0.3	0.3	0.3	1.5	1.5	1.5
ΔT_0 [K]	0	+2	−2	0	+2	−2
Ri	0	+1.1	−1.1	0	+0.04	−0.04
Re	2.9×10^4	2.9×10^4	2.9×10^4	1.4×10^5	1.4×10^5	1.4×10^5
Gr	–	9.2×10^8	9.2×10^8	–	9.2×10^8	9.2×10^8

mentioned in Section 2.2. The buildings are cubes with edge $H = 1.5$ m at a distance H from each other and are exposed to a constant turbulent airflow. Following the classification by Oke et al. (2017), an isolated roughness flow regime is developed in the open square, while between the buildings, a skimming flow regime is established.

Six configurations are simulated by varying the airflow reference velocity and the temperature difference between the waterbody and the surrounding air. The reference velocity at building height is set to $U_0 = 1.5$ m/s to achieve a forced-convection regime, where the system is dominated by the airflow motion, while a value of $U_0 = 0.3$ m/s is used to obtain a mixed-convection regime, where airflow and convective motions are comparable. Reynolds independence was achieved as in both cases $Re > Re_c$, where $Re_c = 11{,}000$ for flows across street canyons with $H/W = 1$ (Chew et al., 2018). The temperature difference is set to $\Delta T_0 = +2$ for a warmer waterbody and upward convection and $\Delta T_0 = -2$ for a cooler waterbody and downward convection. In addition, a baseline configuration without the waterbody is reproduced as a benchmark case. Table 2 summarises the six simulations under consideration and reports the relative dimensionless numbers: simulations where the waterbody is absent (baseline), warmer (warm) and cooler (cool) than the air are performed for forced- and mixed-convection regimes.

This study assumes neutral atmospheric stability as an initial approach. It is worth noting though that atmospheric stratification is common in urban areas and can affect the flow, turbulence and temperature fields (Kanda and Yamao, 2016; Marucci and Carpentieri, 2020). Moreover, building and ground surfaces are modelled with equal and uniform temperature values. Although this is not representative of a daytime situation when building and ground surfaces can reach high temperatures, field measurements have shown that urban street canyons are mostly isothermal during the night (Di Sabatino et al., 2020). Hence, although a realistic representation of the urban environment in terms of surface temperatures and atmospheric stability is not within the scope of this study, it is safe to assume that the $\Delta T_0 = +2$ cases are typical of a night-time condition. Also, notice that the selected Richardson numbers are consistent with those observed in urban environments (Aliabadi et al., 2019; Di Sabatino et al., 2020).

4.2. Initial and boundary conditions

In all cases, the air is initially at rest, and the atmosphere is neutrally stratified and at a characteristic temperature of $T_a = 298.15$ K (25 °C) and $T_a = 294.15$ K (21 °C) for the cooler- and warmer-waterbody cases, respectively. Assuming constant relative humidity of 60%, the vapour concentration is set to $\omega_a = 0.0119$ for the cooler-waterbody cases and $\omega_a = 0.0093$ for the warmer-waterbody cases. Air and water vapour properties at 25 °C with 60% relative humidity are used for all scenarios. The differences across small ranges of temperature have a negligible impact on the results. Prandtl and Schmidt numbers for all scenarios are $Pr = 0.73$ and $Sc = 0.62$, respectively, whilst their turbulent counterparts are $Pr_t = 0.85$ and $Sc_t = 0.80$.

Boundary conditions are set following the guidelines by Franke et al. (2007) and Tominaga et al. (2008). At the inlet, the profiles for U, k and ε are the ones proposed by Richards and Hoxey (1993) and later revisited by Richards and Norris (2011) for a neutral atmospheric boundary layer:

$$U(z) = \frac{u^*_{ABL}}{\kappa}\ln\left(\frac{z+z_0}{z_0}\right), \quad k(z) = \frac{{u^*_{ABL}}^2}{\sqrt{C_\mu}}, \quad \varepsilon(z) = \frac{{u^*_{ABL}}^3}{\kappa(z+z_0)}, \tag{16}$$

where z is the vertical direction, $z_0 = 0.135$ m is the aerodynamic roughness length (adopted from the roughness length estimation of the outdoor scale model COSMO, whose geometry is similar to the building array used in this study Kanda et al., 2007), u^*_{ABL} the friction velocity, $C_\mu = 0.09$ is a model constant, and $\kappa = 0.4$ is the von Karman constant. The friction velocity is set in such a way to have the desired reference velocity at the building height. Temperature and vapour concentration are assigned the constant values of T_a and ω_a, while pressure enforces a zero-gradient condition. At the outlet, pressure is set to a constant value. For all other variables, an outflow condition is employed, assuring a zero-gradient condition if the flow exits the domain, and a zero value in a case of backward inflow (see the implementation of `inletOutlet` condition in OpenFOAM). At the top, the velocity field enforces a constant shear-stress $\tau = \rho {u^*_{ABL}}^2$, as proposed by Hargreaves and Wright (2007) to assure horizontal homogeneity of the velocity profile. The other quantities have a zero-gradient condition. At the lateral boundaries, a symmetric condition is applied to all variables.

The ground and buildings are modelled as solid boundaries, with the buildings considered smooth surfaces with zero roughness (Ricci and Blocken, 2020). A similar approach has been adopted for the water surface. The no-slip condition is applied to the velocity field, zero-gradient

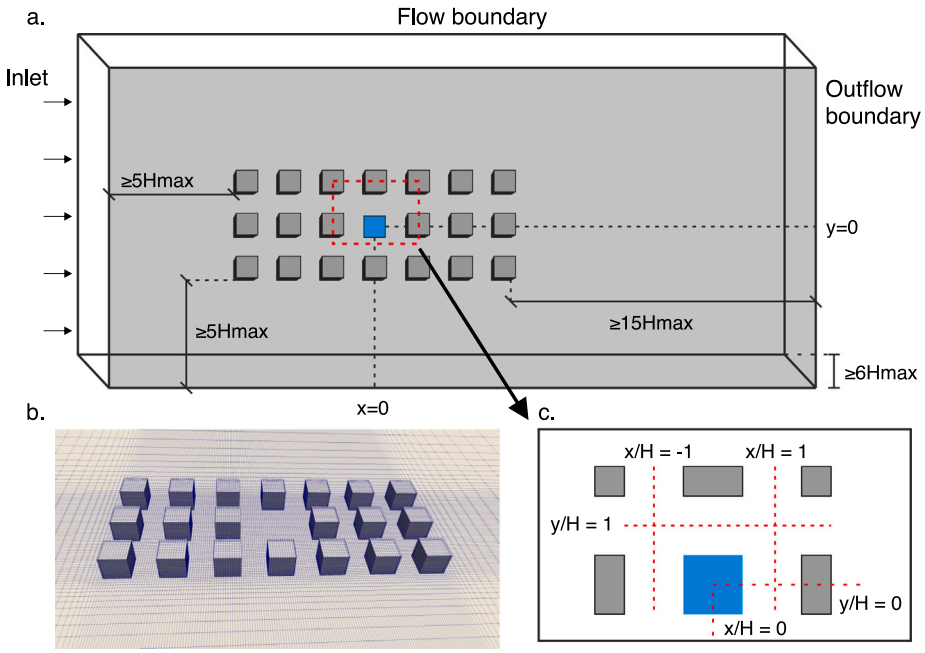

Fig. 5. Overview of the case study geometry and computational grid: (a) schematic representation of the case geometry; (b) sketch of the computational grid; (c) sampling lines used for the analysis of the results.

is used for pressure, and wall functions are utilised for turbulent quantities. Particularly, for ν_t, the function for smooth surfaces `nutkWallFunction` is applied to buildings and waterbody, while the function reproducing the atmospheric boundary layer `atmNutkWallFunction` is applied to the ground. For k and ε, respectively, the functions `kqRWallFunction` and `atmEpsilonWallFunction` are enforced at every surface. See the ESI-OpenCFD (2006) documentation for implementation details. For $\alpha_{T,t}$ and $\alpha_{\omega,t}$, specific wall functions are implemented (as described in Section 2.3) and applied to all surfaces. The temperature of the ground and buildings is set equal to the ambient temperature T_a, while the waterbody temperature is kept constant at $T_w = 296.15$ K (23 °C). For vapour concentration, a zero-gradient condition is set at ground and buildings, whist for the waterbody is set to $\omega_w = 0.0175$.

4.3. Computational domain and grid independence study

The dimensions of the computational domain are chosen following the guidelines by Franke et al. (2007) to ensure that the lateral boundaries are located far enough from the buildings and avoid possible interactions (Blocken, 2015). The distance of the building array from the inlet is $5H$, from the lateral boundaries is $7.5H$, from the top boundary is $5H$, while from the outlet is $15H$ so that a fully developed wake flow can be achieved. The final dimensions of the domain are $33H \times 35H \times 6H$ in the streamwise, spanwise and vertical directions. Fig. 5a sketches the domain geometry. This configuration ensures that the blockage ratio BR, i.e. the ratio of the total projected frontal area of the buildings to the domain cross-section area, is $BR < 3\%$ (Franke et al., 2007; Tominaga et al., 2008), and the directional blockage ratio, i.e. the decomposition of BR in the streamwise and spanwise direction, is $BR_i < 17\%$ as recommended by Blocken (2015). Particularly, the blockage ratio is $BR = 2.4\%$, while the directional blockage ratio is $BR_y = 14.3\%$ in the spanwise direction and $BR_z = 16.7\%$ in the vertical direction.

The computational grid consists of a Cartesian, orthogonal and structured mesh consisting of $191 \times 128 \times 37$ cells for a total of 846,976 cells. The grid is refined near the buildings to ensure a better spatial resolution in the region of interest; see Fig. 5b. Near the solid surfaces, the first computational cell is placed at a dimensionless wall distance of $y^+ = yu_\tau/\nu > 30$ (where y is the wall-normal direction and u_τ is the friction velocity). This required the use of wall functions for the accurate resolution of the wall-boundary layer (Blocken et al., 2007).

A grid independence study is conducted to assess the quality of the selected mesh. Three meshes are analysed: (i) the medium mesh as described above; (ii) the coarse mesh having a 50% cell reduction in every direction, composed of 252,160 cells and with a refinement ratio of $r = 1.9$; (iii) the fine mesh having a 50% cell increase in every direction, composed of $2,923,568$ cells and with a refinement ratio of $r = 1.8$. The representative cell length h – defined as the average cell width estimated as the cube root of the cell volume – for the coarse, medium and fine meshes is $h = 0.141H$, $0.074H$, $0.040H$, respectively. Hence, the representative cell length difference is more than 30% as recommended by Celik et al. (2008).

The target variables of the mesh independence study are mean values of dimensionless streamwise velocity U/U_0 and TKE k/U_0^2. In Fig. 6, the target variables computed along a vertical line at the centre of the domain ($y/H = x/H = 0$) from the ground to roof level ($0 \leq z/H \leq 1$) are plotted against the representative cell lengths of the three meshes. Using Richardson Extrapolation, the solution of an infinitely fine mesh is estimated based on the values from the medium and fine mesh and is shown for $h = 0$. Both quantities experience oscillatory convergence with the medium and fine meshes reporting values close to the solution with $h = 0$. For an error estimate between the values of the medium and fine mesh, the Grid Convergence Index (GCI) proposed by Roache (1994, 1997) is employed. GCI values for the streamwise velocity and TKE are 0.6% and 0.3%, respectively, indicating that the medium mesh provides nearly grid-independent results.

5. Results and discussion

For each simulated scenario (see Table 2), the impact of the waterbody on the overall circulation in the urban neighbourhood is investigated by analysing the mean velocity field, and the temperature and vapour concentration. Horizontal profiles and contours are extracted at pedestrian level ($z/H = 0.23$), corresponding to 1.75 m at full scale (Moonen et al., 2012; Ramponi et al., 2015). The position of the sampling lines is depicted in Fig. 5c. Turbulence effects are studied through the turbulent kinetic energy, and a focus

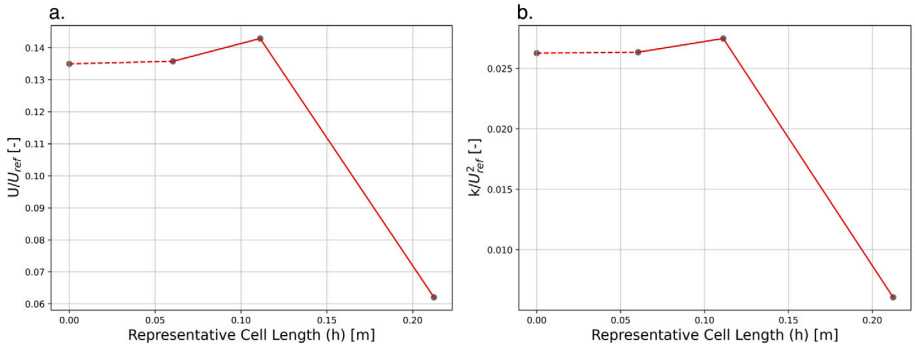

Fig. 6. Results of the mesh convergence study for mean values of (a) streamwise velocity ratio U/U_0 and (b) normalised turbulent kinetic energy k/U_0^2 along a vertical line $0 \leq z/H \leq 1$ at $y/H = 0$ and $x/H = 0$.

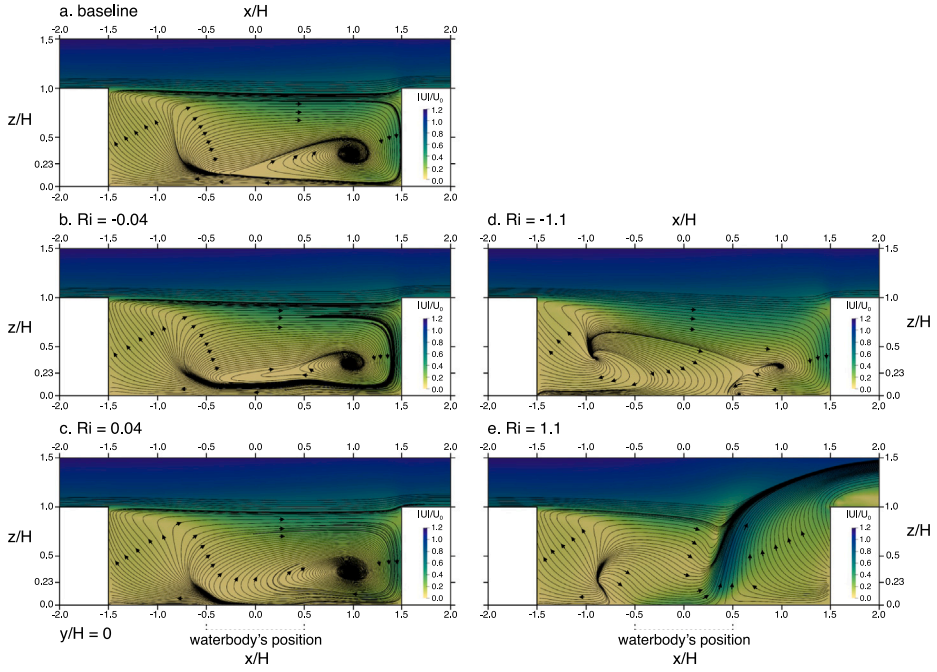

Fig. 7. Velocity streamlines for the cases under forced convection ($Ri = \pm 0.04$) and mixed convection ($Ri = \pm 1.1$) over a vertical plane at $y/H = 0$ in the open square ($-1.5 \leq x/H \leq 1.5$). (a) baseline scenario; (b) cooler waterbody with $Ri = -0.04$; (c) warmer waterbody with $Ri = 0.04$; (d) cooler waterbody with $Ri = -1.1$; (e) warmer waterbody with $Ri = 1.1$. The normalised velocity magnitude is depicted spatially in the background.

on the exchange processes at the interface between buildings and the surrounding atmosphere is presented.

Three critical regions of interest are identified and used in the discussion that follows: (i) The open square, the area above and around the waterbody: $-1.5 \leq x/H \leq 1.5$ and $0 \leq y/H \leq 0.5$; (ii) Downwind canyons, the first and the second street canyon (in spanwise direction) downwind to the waterbody. DC1: $2.5 \leq x/H \leq 3.5$ and $0 \leq y/H \leq 0.5$; DC2: $4.5 \leq x/H \leq 5.5$ and $0 \leq y/H 0.5$; (iii) The street canyon, with the axis in the streamwise direction, placed at the side of the open square: $-2.5 \leq x/H \leq 6.5$ and $0.5 \leq y/H \leq 1.5$.

5.1. Mean velocity field at vertical sections

Fig. 7a, b, c shows the non-dimensional velocity streamlines and the velocity magnitude under forced convection ($Ri = \pm 0.04$) over a vertical plane passing from the centre of the open square, at $y/H = 0$. Fig. 7a displays the baseline scenario without the waterbody. The open square is dominated by a principal vortex induced by the atmospheric wind, which is a characteristic feature of an isolated roughness flow (Coceal et al., 2006). The vortex extends in the range $-0.6 \leq x/H \leq 1.5$, dominating the dynamics in the above-waterbody area ($-0.5 \leq x/H \leq 0.5$) and downwind–waterbody area ($0.5 \leq x/H \leq 1.5$) where the centre is located at about $x/H = 1.0$ and $z/H = 0.33$. At the ground of the open square, approximately in the range $0 < z/H < 0.1$, a reverse flow develops in the negative x-direction. This flow is then deflected upwards in the upwind–waterbody area ($-1.5 \leq x/H \leq -0.5$), characterised by an ascending flow that guides the air towards the interface with the free atmosphere at roof level ($z/H = 1$). Fig. 7b, c reports the cases with the cooler ($Ri = -0.04$) and warmer ($Ri = 0.04$) waterbody under forced convection. Due to the predominance of the inertial forces over the convective ones, the presence of the waterbody has minimal effects on the flow structure in the open square. In the cooler-waterbody case, the height of the reverse-flow zone near the ground is slightly extended up to $z/H = 0.15$. In the warmer-waterbody case, a weak upward buoyant flow is generated above the waterbody, enhancing the principal vortex motion and relocating its centre slightly higher at $z/H = 0.35$. The reverse-flow zone in the upwind–waterbody area remains unaffected.

Fig. 7d, e displays the non-dimensional velocity magnitude and streamlines for the cases under mixed convection ($Ri = \pm 1.1$) over a vertical plane at $y/H = 0$ in the open square. The flow structure of the baseline scenario is similar to the one under forced convection,

as both Reynolds numbers are high enough, i.e. $Re = 1.4 \times 10^5$ and $Re = 2.9 \times 10^4$ for forced and mixed convection, respectively (Allegrini et al., 2013). Therefore, we refer to the discussion of Fig. 7a. In Fig. 7d, the downward convection caused by the cooler waterbody ($Ri = -1.1$) results in the rise of a downward motion in the above-waterbody area. The downward motion impinges the water surface and is subsequently directed to the upwind–waterbody area. Consequently, the reverse flow that develops near the ground in the baseline scenario is interrupted and the principal vortex is significantly reduced, mainly confined in the downwind–waterbody area. In Fig. 7e, the buoyancy force generated by the warm and less dense air above the warmer waterbody triggers a strong upward motion at $0.3 \leq x/H \leq 0.5$ in the above-waterbody region. The upward motion extends beyond the roof level, inducing a vertical thermal plume advected by the main flow, causing cooler and more dense air being drawn from the surroundings into the open square. This is in qualitative agreement with the wind tunnel study conducted by Tsalicoglou et al. (2020) on the impact that a street canyon's ($H/W = 0.8$) heated surfaces have on airflow. The authors found that the principal vortex within the canyon weakens and eventually breaks up with increasing Richardson numbers. In the downwind–waterbody area, the principal vortex is destroyed, while the ascending flow is still present in the upwind–waterbody area.

Globally, it has been found that the waterbody effects under forced convection are very weak and do not significantly alter the overall dynamics of the system. This is consistent with the findings of the wind tunnel experiments conducted by Kovar-Panskus et al. (2002) and Allegrini et al. (2013) employing heated ground and/or building surfaces. Hence, the discussion that follows focuses only on mixed convection.

Fig. 8 shows the flow structure in the downwind canyons and how it is affected by introducing a warmer waterbody under mixed convection ($Ri = 1.1$). The effects of the $Ri = -1.1$ case are negligible and, thus, are not shown. Fig. 8a depicts the baseline scenario, where the dynamics of both DC1 and DC2 canyons are dominated by a clockwise vortex, centred at the top-right part of the canyon. This is generated and maintained by the downward transfer of momentum from the above-roof region (Kim and Baik, 2005) and is a characteristic feature of the skimming flow regime (Allegrini et al., 2013; Kim and Baik, 1999). As a result, the air within the canyon flows clockwise and is separated from the above-roof flow ($z/H > 1$). Fig. 8b shows the warmer-waterbody case, where the thermal plume influences the circulation in the downwind canyons by altering the skimming flow structure. Notably, the clockwise vortex is destroyed and the in-canyon flow is no longer separated from the atmospheric one. Presumably, this indicates a higher exchange of momentum and mass between the canyon and the surrounding atmosphere. Such a feature is of particular interest, suggesting an enhancement of the pollutant removal from the urban canyons.

In Fig. 9, the profiles of dimensionless streamwise velocity are plotted along three vertical lines within the open square ($y/H = 0$): in the upwind–waterbody area, $x/H = -1.13$; in the above-waterbody area, $x/H = 0$; in the downwind–waterbody area, $x/H = 1.13$. Additionally, two vertical lines are employed at the centre of the downwind canyons. Globally, the forced-convection profiles ($Ri = \pm 0.04$) collapse to those of the baseline scenario. This supports our observation that the presence of the waterbody under forced convection is irrelevant to the overall dynamics. In Fig. 9a, it is demonstrated that for the upwind line, the velocity profile is the same for all cases with near-zero negative values, suggesting that the influence of the waterbody is minimal in the upwind–waterbody region. For the centre line, all profiles, apart from the $Ri = 1.1$ case, show weak negative velocities close the ground, whilst beyond $z/H = 0.2$, increasing positive values can be observed. The $Ri = -1.1$ case shows slightly higher velocities above $z/H = 0.4$ that can be attributed to the downward motion induced by the presence of the cooler water surface. For the $Ri = 1.1$ case, positive values are observed close to the ground, as the buoyant plume draws air from the surroundings (see Fig. 7e). Negative velocity values are present close to the ground for the downwind line, whilst increasing positive values are observed beyond about $z/H = 0.3$. For the $Ri = 1.1$ case, negative values are maintained almost until roof level. In the downwind canyons (Fig. 9b), similar behaviour is observed for all cases: negative values close to the ground due to the clockwise vortex and increased positive values near the roof level. The $Ri = 1.1$ case exhibits slightly weaker values along the entire vertical line, as the principal vortex has been destroyed.

5.2. Mean velocity field at horizontal sections

In Fig. 10, the dimensionless velocity magnitude and streamlines are depicted in the streamwise street canyon over a horizontal plane at pedestrian level. Only the baseline and $Ri = 1.1$ cases are reported and discussed, as the impact of the waterbody in the other cases is negligible. Fig. 10a shows the baseline case. As expected, the main flow is directed downwind, and air flows from the canyons at $1.5 \leq y/H \leq 2.5$ inside the street canyon. A small anti-clockwise vortex is formed with its centre located at $x/H = 0.1$, $y/H = 1.1$, while a second vortex is detectable within the open square. In both the downwind canyons, DC1 and DC2, a small clockwise vortex is generated near the upwind building facade. The canyons are mostly isolated from the main flow. However, weak inflow is observed in DC2, which is, presumably, a local form of lateral channelling due to the re-attachment of the flow after the change of the flow pattern in the open square (Princevac et al., 2010). This lateral flow has been found to have positive effects on the canyon's ventilation, especially for cases where buildings are aligned to the direction of the wind (Ramponi et al., 2015). Fig. 10b reports the warmer-waterbody case. The strong ascending flow is detectable in the zone of high-velocity magnitude above the waterbody, altering the dynamics in the open square. As a result, airflow is drawn towards the waterbody to replace the air that has moved upwards. In the downwind canyons, the disruption of the skimming flow causes air from the main flow to be drawn inside the canyons, leading to the formation of a larger clockwise vortex in the upwind part of the canyons. This means that an enhancement of the lateral channelling is observed, contributing more to the canyons' ventilation.

Fig. 11 presents the dimensionless streamwise and vertical velocity profiles within the open square and downwind canyons over the domain's centreline ($y/H = 0$) at pedestrian level. In the open square (Fig. 11a), the streamwise velocity profiles for the baseline and forced-convection scenarios collapse on the same line. Mostly negative values are observed along the entire line, with near-zero positive values above the waterbody. Similar behaviour is observed for the $Ri = -1.1$ case with slightly weaker values above and downwind of the waterbody. For the warmer-waterbody case, the strong vertical motion leads to increased positive values in the upwind and above-waterbody area, whilst higher negative values are present in the downwind part. In the downwind canyons (Fig. 11c), the profiles of all cases, apart from the $Ri = -1.1$ case, are similar. Streamwise velocity values are negative, indicating a reverse flow that dominates the entire canyon width. For the $Ri = -1.1$ case, slightly higher negative values can be observed in the centre of the canyons. In Fig. 11b, the vertical velocity profiles in the open square are reported. Apart from the case with a warmer waterbody, similar behaviour is observed for the rest. High negative values are present near the downwind building's facade as per the direction of the principal vortex (see Fig. 7a–d), whilst near-zero positive values are present in the rest of the open square. Weak positive values are present near the upwind building, implying an ascending flow. The higher values of vertical velocity close to the downwind building, compared to other parts of the open square, explain the formation of the principal vortex at the bottom-right location (Baik and Kim, 2002). The downward convection in the $Ri = -1.1$ case leads to weak negative values above the waterbody, probably due to the thermal-vapour stratification, which hampers the upward motion (see the discussion for

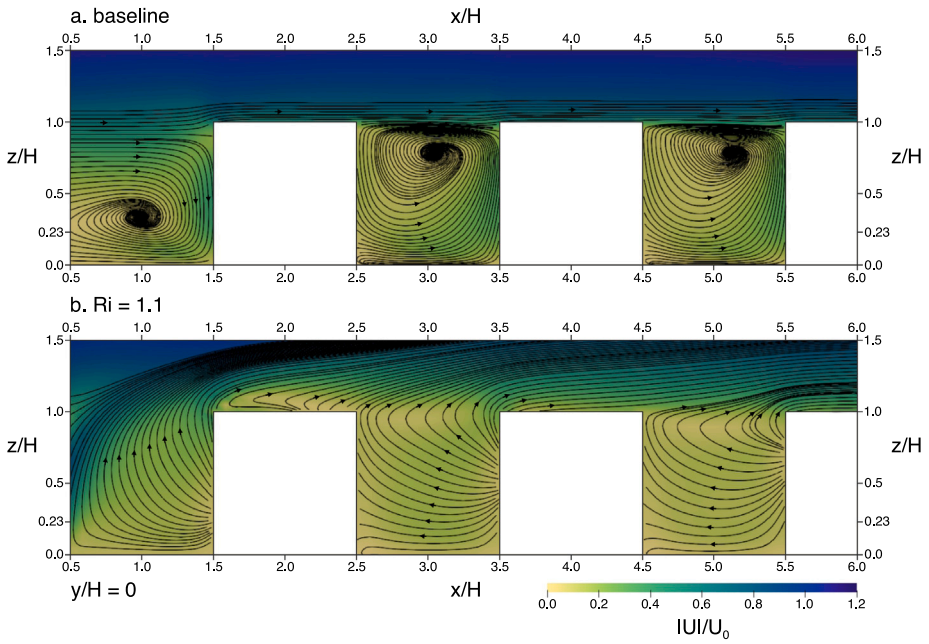

Fig. 8. Velocity streamlines for (a) the baseline scenario without the waterbody and (b) the warmer-waterbody case under mixed convection ($Ri = 1.1$) over a vertical plane at $y/H = 0$ in the downwind canyons ($-0.5 \leq x/H \leq 7.5$). The normalised velocity magnitude is depicted spatially in the background.

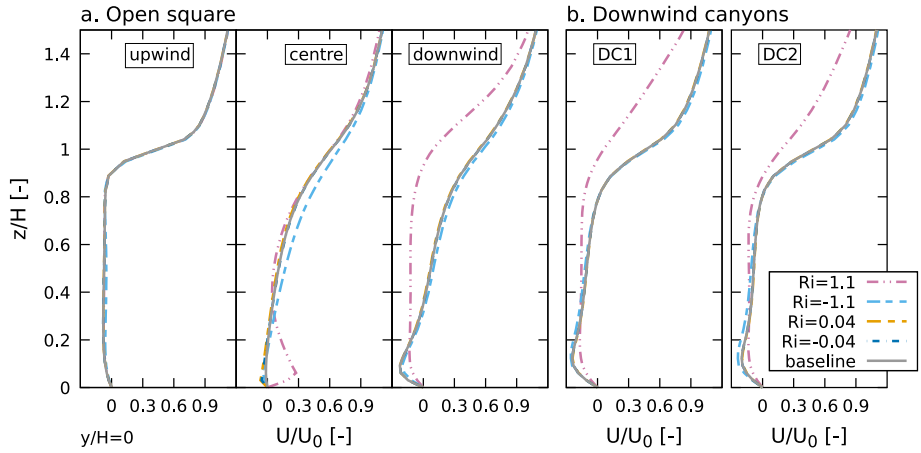

Fig. 9. Normalised streamwise velocity (U/U_0) along three vertical lines within the open square (upwind: $x/H = -1.13$; centre: $x/H = 0$; downwind: $x/H = 1.13$) and in the downwind canyons (located in the centreline of DC1: $x/H = 3$, and DC2: $x/H = 5$) at $y/H = 0$.

Fig. 13). As expected, the thermal plume in the $Ri = 1.1$ case induces high positive values above the waterbody, whilst the destruction of the principal vortex (see Fig. 7e) leads to an ascending flow in the upwind part. The profile remains unaffected in the upwind–waterbody region. In the downwind canyons (Fig. 11d), the profiles of all cases, apart from the $Ri = 1.1$ case, collapse on the same line. Negative values are present close to the downwind building's facade, in accordance with the standing clockwise vortex, whilst weak positive velocities can be observed in the upwind part. A similar profile has been reported experimentally by Allegrini et al. (2013) that, potentially, explains the slight shift of the vortex's centre downwind. For the $Ri = 1.1$ case, the downward flow is considerably decreased to near-zero values as expected from the destruction of the skimming flow regime. Also, the weak positive velocities over the largest part of the canyons corroborate the hypothesis of more effective ventilation.

Fig. 12 shows the normalised streamwise and spanwise velocity profiles over a horizontal line across the middle of the street canyon ($y/H = 1$) at pedestrian level. The profiles of the baseline and forced-convection cases are identical for both velocity components. For the streamwise velocity (Fig. 12a), weak positive values are present in the middle of the open square, whilst increased values can be observed upwind and downwind. As flow is directed further downwind, it decelerates with decreased positive values near the DC2 canyon. For the $Ri = -1.1$ case, streamwise velocity shows negative near-zero values in the centre of the open square, whilst increased values can be observed downwind of the open square ($x/H \geq 1.5$). For the case with a warmer waterbody ($Ri = 1.1$), velocity values experience higher values from the middle of the open square, whilst upwind the profile remains unaffected. In Fig. 12b, the profiles of spanwise velocity are appraised. For the baseline and forced-convection cases, spanwise velocity is primarily negative, with the largest values observed in the upwind–waterbody area and the middle of the DC2 canyon. Positive values can be observed downwind of the waterbody to approximately the DC1 canyon. For the $Ri = -1.1$ case, increased spanwise velocities are observed from the middle of the waterbody to the beginning of the DC1 canyon, whilst decreased negative velocities are present in the DC2 area. The presence of a warmer waterbody leads to negative values throughout the street canyon, with the largest ones found in

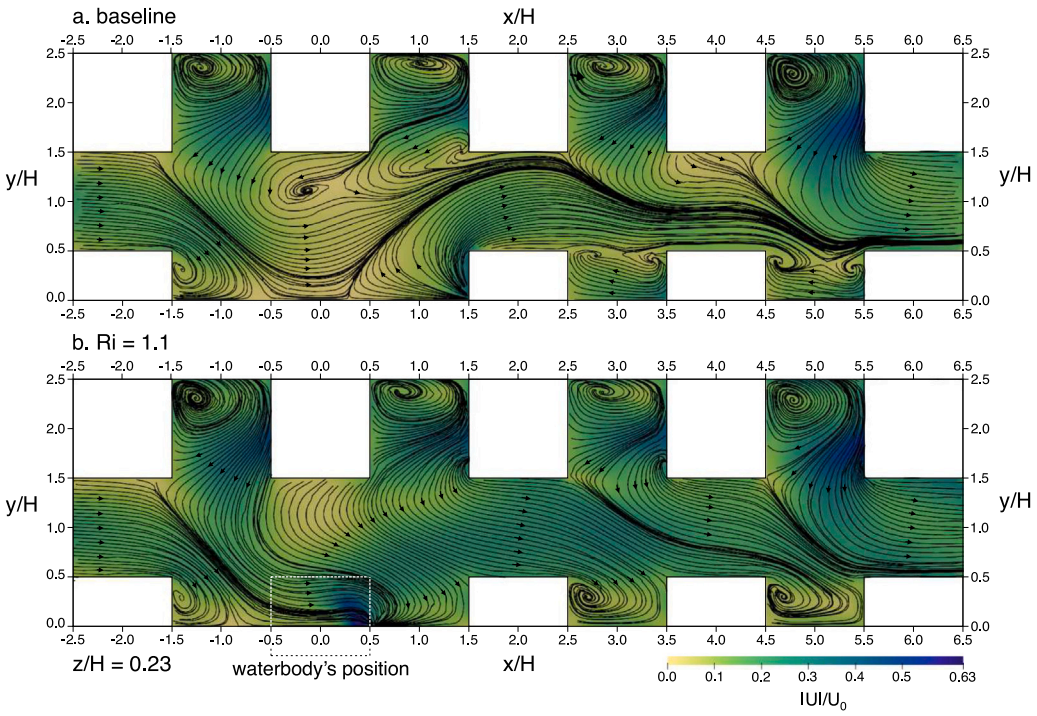

Fig. 10. Velocity streamlines for (a) the baseline scenario without the waterbody and (b) the warmer-waterbody case under mixed convection ($Ri = 1.1$) over a horizontal plane at pedestrian level ($z/H = 0.23$) and within the downwind canyons ($-0.5 \leq x/H \leq 7.5$). The normalised velocity magnitude is depicted spatially in the background.

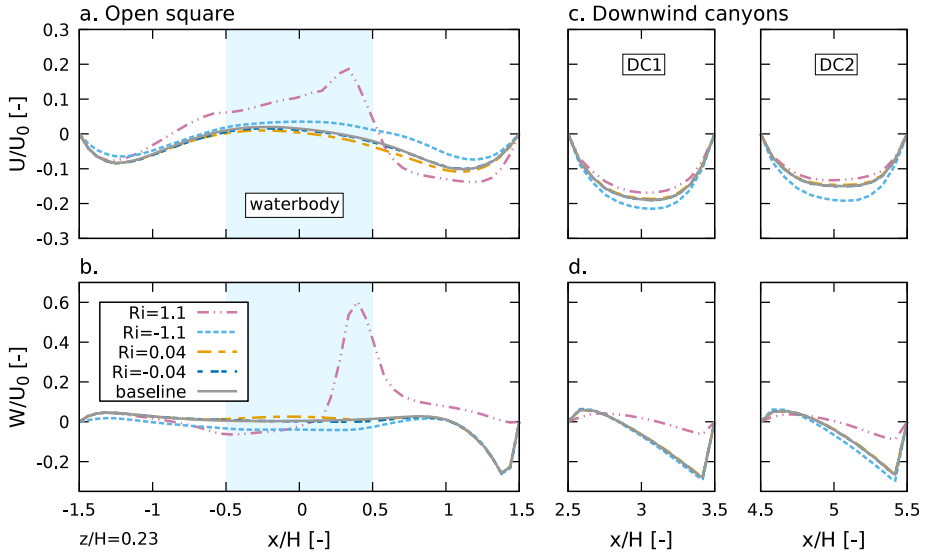

Fig. 11. Profiles of normalised velocity ratios over a horizontal line across the middle of the domain ($y/H = 0$) at pedestrian level ($z/H = 0.23$). (a), (b) Results within the open square ($-1.5 \leq x/H \leq 1.5$) for streamwise (U/U_0) and vertical velocity (W/U_0), respectively; (c), (d) Results within the downwind canyons (DC1: $2.5 \leq x/H \leq 3.5$, DC2: $4.5 \leq x/H \leq 5.5$) for streamwise and vertical velocity, respectively.

the upwind–waterbody area and the downwind canyons. This further corroborates the hypothesis of increased channelling due to the strong vertical plume and the consequent disruption of the skimming flow in the downwind canyons.

5.3. Temperature and vapour concentration

Fig. 13 shows the contours of normalised temperature (T^*) and water vapour (ω^*) over a vertical plane at $y/H = 0$ for forced- and mixed-convection cases. As the results suggest, the profiles of T^* and ω^* are primarily similar, as expected by assuming heat–mass analogy. Hence, for the sake of simplicity, the discussion is focused on T^*, and equal consideration is implied for ω^*. In the forced-convection case, the cooler and warmer waterbody cases lead to similar contour plots; thus, only the warmer case at $Ri = 0.04$ is presented and discussed in Fig. 13a. Temperature exhibits a steep gradient in the above-waterbody area to approximately half of the pedestrian level ($z/H = 0.1$). The fact that the thermal effects are equally distributed around and over the waterbody can be attributed to the near-zero streamwise and vertical velocities seen in Fig. 11 due to the obstruction from the prevailing wind. In Fig. 13b, the cooler waterbody presents a similar behaviour as in the forced-convective cases. Temperature and vapour remain concentrated near the water

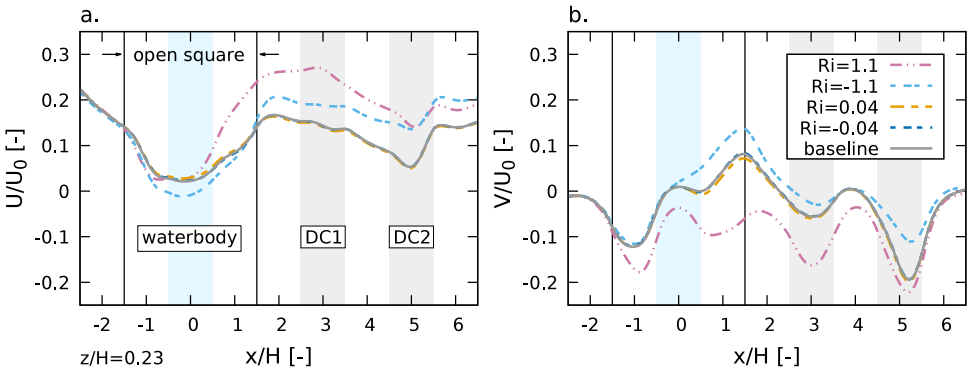

Fig. 12. Profiles of normalised streamwise (U/U_0) (a) and spanwise (V/U_0) (b) velocity over a horizontal line in the middle of the street canyon ($y/H = 1$) at pedestrian level ($z/H = 0.23$). The shaded areas denote the position of the waterbody (blue) and the downwind canyons DC1 and DC2 (grey). The location of the open square is shown with the vertical dotted lines.

surface, where a strong vertical gradient triggers a vertical downward buoyancy force. The general circulation of the open square (see Fig. 7d) transports the scalars in the upwind–waterbody area. In Fig. 13c, the warmer waterbody exhibits a strong vertical temperature/vapour gradient near the water surface, generating an upward buoyancy and the ascending flow that characterised this configuration. The ascending flow transports temperature and vapour, giving rise to a thermal plume that extends above roof level towards the streamwise direction. The upwind–waterbody area remains unaffected by the evaporation process.

In the horizontal section and at pedestrian level, the forced-convection temperature and water vapour effects are localised around the water surface due to the reduced velocities within the open square. Under mixed convection, the cooler waterbody results in a more widely spread impact (up to $y/H = 1.5$) due to the downward motion that directs wind, and thus scalars, more upwind and in the lateral direction. For the $Ri = -1.1$ case, the strong upward buoyant flow creates a steep temperature gradient above the waterbody that, in combination with the increased negative spanwise velocities, minimises the warmer-waterbody effects in the lateral direction.

Fig. 14 depicts T^* profiles over the domain's centreline at pedestrian level. The forced-convection cases have similar absolute values in the open square (Fig. 14a), with the most significant changes observed above the waterbody. The $Ri = -1.1$ case demonstrates a similar behaviour to the one under forced convection, albeit with higher temperature reduction in the upwind–waterbody area, as shown in Fig. 13b. Again, the $Ri = 1.1$ case shows large T^* values over the waterbody, whilst slightly decreased values are observed upwind of the centre of the open square. In the downwind canyons (Fig. 14b), all cases lead to small temperature changes. However, the warmer-waterbody case under mixed convection shows slightly decreased values compared to the forced-convection one, which can be attributed to the enhanced ventilation of the downwind canyons, as previously discussed.

Note that the non-dimensional values T^* and ω^* indicate the percentage change with respect to the reference air–water temperature/vapour difference. In other words, a value of $T^* = 0.05$ implies a temperature increase of 5% of ΔT_0, meaning a 0.1 °C increase when $\Delta T_0 = +2$ °C. In the literature, the effects of different UHI mitigation strategies are usually presented with a single temperature value without indicating the temperature differential. While this might be accurate enough to describe the influence of green space and high albedo materials, it might be misleading when dealing with waterbodies. In contrast with other UHI mitigation strategies, the properties of water and, thus, its overall effect vary in time depending on the background climate, the time of the day and its morphological parameters, e.g. size, shape, depth.

Imam Syafii et al. (2017), in their reduced-scale physical model, whose configuration is similar to the building array of this study, report air temperatures with and without the presence of a small pond at $z/H = 0.2$ above the water surface. Their reported values are made dimensionless according to Section 2.5 and used for comparison. From 7:00 to 21:00, the average temperature difference between the air and water surface was $\Delta T = -2$ °C, leading to a normalised temperature decrease of $T^* = -0.3$. Similarly, Theeuwes et al. (2013) simulated a temperature decrease due to the presence of a lake with 15 °C water temperature of about 1.2 °C at 10:00 when the air–water temperature difference was approximately $\Delta T = -3.4$ °C. When this gets non-dimensionalised, the equivalent temperature reduction is about $T^* = -0.35$. The results of these studies are slightly higher than the values presented in Fig. 14a at a similar height, i.e. $T^* = -0.25$ and $T^* = -0.22$ for forced and mixed convection, respectively. The discrepancies can be explained by the increased wind speeds and the favourable alignment of the waterbodies with the prevailing wind. In fact, the positioning and geometry of the waterbodies play a significant role on the overall thermal behaviour (Ampatzidis and Kershaw, 2020; Sun and Chen, 2012). Here, we have isolated the waterbody from the prevailing wind, leading to decreased mixing in the open square.

5.4. Turbulent kinetic energy

Fig. 15 shows the distribution of normalised TKE over a vertical section at the domain's centreline. The results of the baseline, forced-convection and $Ri = -1.1$ cases show almost similar behaviour and, thus, only the baseline and the $Ri = 1.1$ cases are presented. For the baseline scenario (Fig. 15a), a steep gradient of TKE exists near the downwind building's facade, where due to the principal vortex, increased vertical velocities are observed. Due to the increased shear, the largest values are located at the downwind building's edge at roof level. In Fig. 15b, the induced vertical motion by the presence of the warmer waterbody leads to the formation of a steeper gradient of TKE above the waterbody and over the roof level. The values in the downwind–waterbody area are decreased, whilst the effect upwind is negligible.

Fig. 16 shows the profiles of TKE (k/U^2_{Ref}) over a horizontal line across the domain's centreline in the open square and downwind canyons. Results are taken at pedestrian (a, c) and roof level (b, d). At the pedestrian level (Fig. 16a), TKE profiles of the baseline and forced-convection cases exhibit identical behaviour. TKE is increasing towards the streamwise direction with the highest values near the downwind building's facade, according to the velocity profiles in Fig. 11. For the $Ri = -1.1$ case, increased values are observed above and downwind of the waterbody, attributed to the downward motion induced by buoyancy. For the $Ri = 1.1$ case, the strong vertical motion leads to increased values upwind and above the waterbody, whilst the destruction of the principal vortex and the decreased vertical velocities close to the downwind building lead to a reduction of TKE in the downwind part.

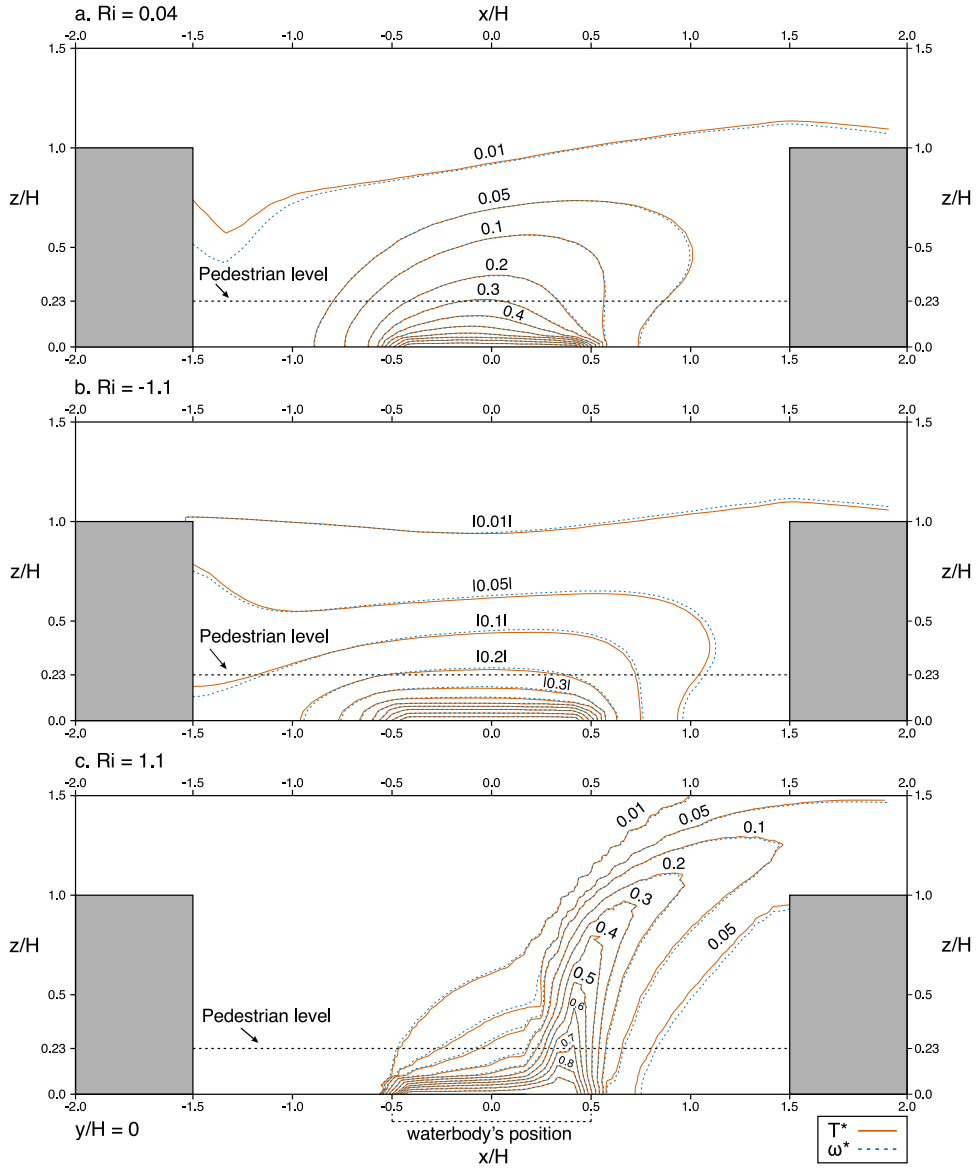

Fig. 13. Contours of normalised temperature (T^*) and water vapour concentration (ω^*) over a vertical plane in the middle of the domain ($y/H = 0$) for forced- and mixed-convection cases. Results for (a) forced convection and warmer waterbody $Ri = 0.04$; similar contours but with negative values are developed with a cooler waterbody but not shown for simplicity, (b) mixed convection and cooler waterbody $Ri = -1.1$; the modulus indicates negative values for temperature decrease and positive values for vapour concentration increase, (c) mixed convection and warmer waterbody $Ri = 1.1$.

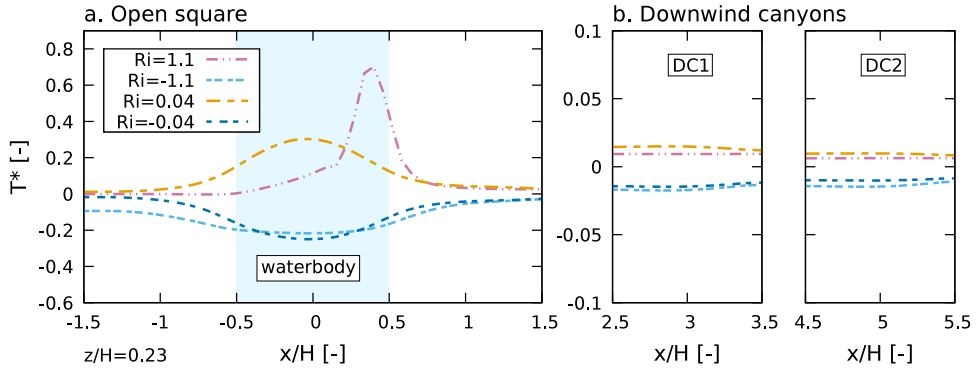

Fig. 14. Normalised temperature (T^*) profiles over a horizontal line in the middle of the domain ($y/H = 0$) at pedestrian level ($z/H = 0.23$). Results for (a) the open square and (b) the downwind canyons.

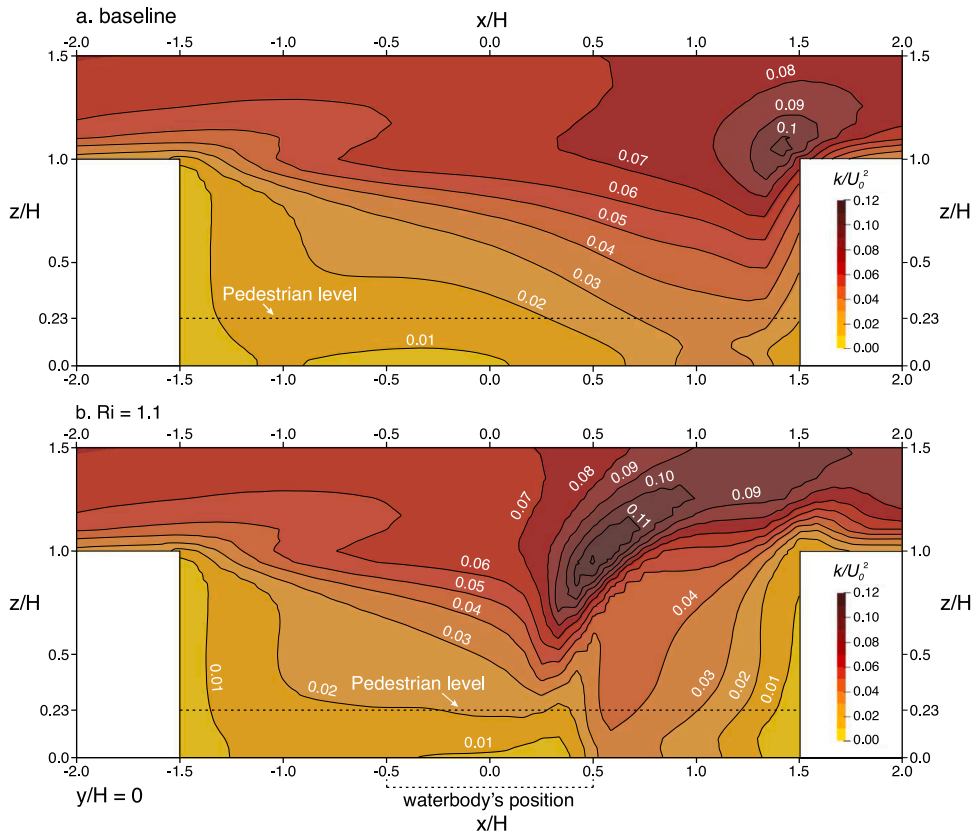

Fig. 15. Contours of normalised turbulent kinetic energy (k/U_0^2) in the open square over a vertical plane across the domain's centreline ($y/H = 0$). Results for (a) baseline scenario without the waterbody; (b) warmer-waterbody case under mixed convection ($Ri = 1.1$).

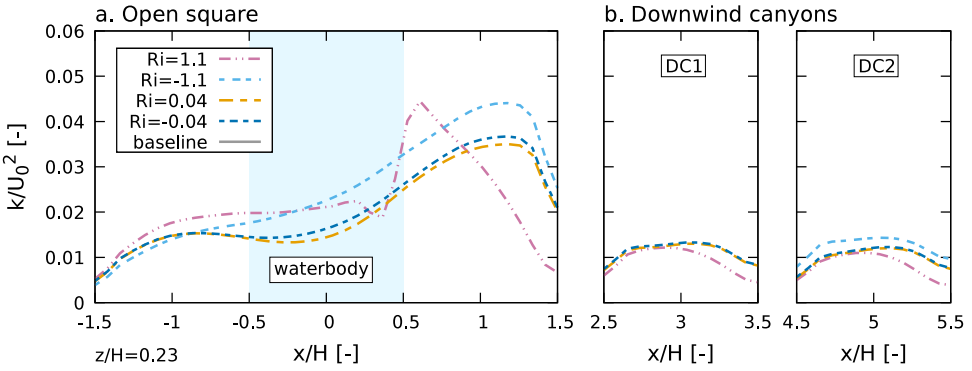

Fig. 16. Profiles of normalised turbulent kinetic energy (k/U_0^2) over a horizontal line across the domain's centreline ($y/H = 0$) at pedestrian level ($z/H = 0.23$) in (a) the open square and (b) the downwind canyons.

In the downwind canyons (16b), apart from $Ri = 1.1$, all cases show similar profiles, with generally low TKE values. The $Ri = 1.1$ case presents lower values in the downwind part as the disruption of the skimming flow has led to decreased vertical velocities (see Fig. 11).

5.5. Interface exchange

The mass exchange between the open square and the surrounding atmospheric flow is shortly addressed by analysing the vertical kinematic fluxes at roof level. The equation of the budget for such fluxes reads:

$$\langle uw \rangle = UW + \langle u'w' \rangle, \tag{17}$$

where the capital letters indicate mean quantities, e.g. $U = \langle u \rangle$. In an attempt to estimate the turbulent contribution to the fluxes, the turbulent $k-\varepsilon$ turbulent model is used to express $\langle u'w' \rangle = -\nu_t(\partial U/\partial z + \partial W/\partial x)$. Both the mean and turbulent terms are computed and reported separately.

Fig. 17 shows the non-dimensional profiles of vertical velocity, TKE and flux budget over a horizontal line at roof level across the domain's centreline. The profiles of the baseline and forced-convection cases are almost identical and, thus, only the results from the former are considered. In the open square, the $Ri = -1.1$ case demonstrates a vertical velocity profile similar to the baseline one, albeit with slightly higher negative values, indicating weak downward motion. For the warmer-waterbody case, a significant increase of vertical velocities is observed downwind of the waterbody due to the strong thermal plume. This effect is also prominent in the downwind canyons (Fig. 17b). For TKE (Fig. 17c, d), the presence of a warmer waterbody leads to increased values at the downwind edge of the water surface, whilst

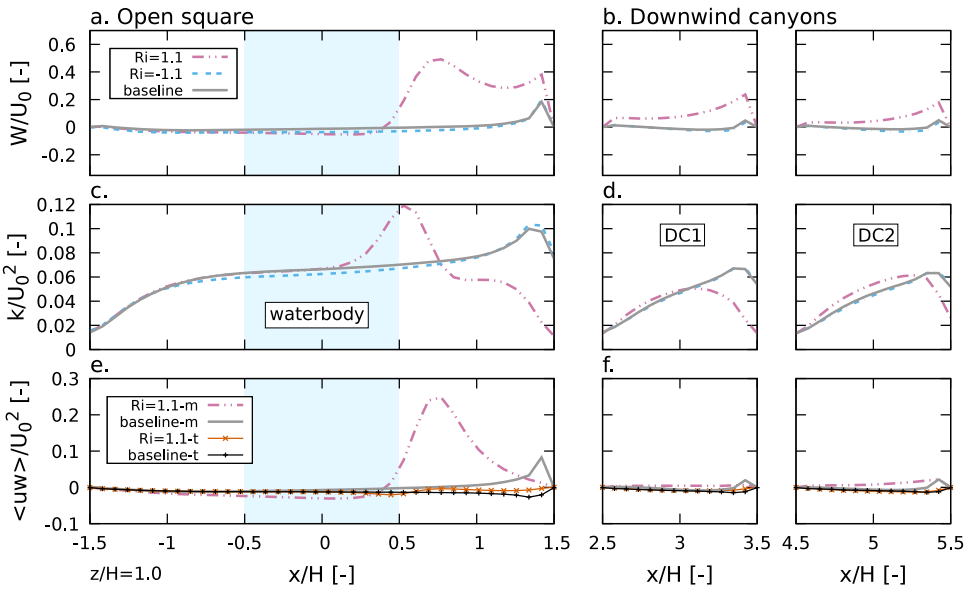

Fig. 17. Profiles of non-dimensional (a, b) vertical velocity, (c, d) TKE and (e, f) vertical flux budget over a horizontal line at roof level ($z/H = 1$) across the domain's centreline ($y/H = 0$). Results for (a, c, e) the open square and (b, d, f) the downwind canyons [$-m$ denotes mean values; $-t$ denotes turbulent values].

a reduction of TKE can be observed close to the downwind building. In the downwind canyons, high values of TKE are observed near the downwind building's edge for all cases, except for $Ri = 1.1$, where the thermal plume has decreased the shear at roof level and shifted the TKE profile upwind.

In Fig. 17e, f, the vertical momentum fluxes for the baseline and warmer-waterbody cases are appraised. As previously shown, the forced-convection and $Ri = -1.1$ cases have a negligible impact at roof level. In the open square (Fig. 17e), the baseline scenario shows mostly weak negative values of vertical exchange above and upwind of the waterbody. In the downwind part, positive values of the mean term are observed with a high peak near the stagnation point at the downwind building's facade, whilst the turbulent counterpart shows weak negative values. For the warmer-waterbody case, a significant increase of mean vertical fluxes is observed right downstream of the waterbody due to the strong vertical motion, indicating intense vertical exchange. On the contrary, the turbulent counterpart shows near-zero values across the entire length of the open square. In the downwind canyons (Fig. 17f), the baseline case exhibits a qualitatively similar profile to the one in the open square. For the warmer waterbody, vertical exchanges by the turbulent flow are mostly unaffected, whilst the destruction of the skimming flow regime and the resulting upward motion has led to positive mean values across the entire canyon length, indicating enhanced mean vertical exchange.

6. Conclusions

This study demonstrates the influence of a blue space on airflow, temperature and vapour concentration distribution in a simplified urban environment. The use of a novel solver that captures evaporation effects has provided new insight into the interaction of blue spaces with their urban surroundings. Simulations were performed under neutral atmospheric conditions for different convection regimes by varying the reference wind speed and the temperature difference between the waterbody and the air above. The results presented here are in qualitative agreement with studies conducted on heated ground and/or building surfaces, showing that the impact of forced convection on the flow structure is minimal compared to the effects of mixed-convection regimes, which promote mixing and increased wind speeds, both within the open square and downwind canyons.

A unique feature of the warmer-waterbody case under mixed convection, which can be considered being representative of nocturnal conditions, is the destruction of the skimming flow regime in the downwind canyons. Presumably, this is an indication that during the night, a warmer waterbody can promote the dispersion and vertical mixing of pollutants from within the urban canopy layer to the atmosphere above by enhancing lateral and vertical ventilation not only in the immediate surroundings of the waterbody but also further downwind.

The evaluation of temperature and vapour concentration distribution has shown that under forced convection, blue space effects are localised, affecting mostly the area above and around the water surface. Under mixed convection, the impact of a cooler waterbody appears more spatially distributed, whereas the introduction of a warmer waterbody creates a strong vertical buoyant flow that extends above roof level and, thus, the effects are not so spatially spread within the urban context. This indicates that blue infrastructure, comprising networks of waterbodies throughout an urban area, can potentially promote the vertical transport of heat and significantly alleviate air pollution within the anthroposphere, which is in agreement with Theeuwes et al. (2013). However, this positive effect would have to be balanced against the daytime hours where the waterbody is cooler (Ri = −1.1) and the potential accumulation of water vapour within the street canyons, the associated increase in humidity and the risk this poses to human thermal comfort, particularly during hot still weather, typical of heatwave events.

The current study was not explicitly designed to address the changes of water temperature due to energy gains or losses. Instead, an isothermal waterbody was considered. Radiation and the resulting varying surface temperatures of buildings, ground and water surfaces were also ignored. Therefore, future studies are needed to focus on the influence of the in-canyon surface temperature differences, especially when recent research has shown that the effect of non-isothermal conditions is particularly present under high Richardson numbers (Chen et al., 2020).

CRediT authorship contribution statement

Petros Ampatzidis: Conceptualization, Formal analysis, Investigation, Methodology, Software, Validation, Visualisation, Writing – original draft, Writing – review & editing. **Carlo Cintolesi:** Methodology, Software, Writing – review & editing. **Andrea Petronio:** Methodology, Software. **Silvana Di Sabatino:** Supervision. **Tristan Kershaw:** Conceptualization, Supervision, Writing – review & editing.

Declaration of competing interest

The authors declare that they have no known competing financial interests or personal relationships that could have appeared to influence the work reported in this paper.

Data availability

Data will be made available on request.

Acknowledgements

The authors would like to express their gratitude to Damogran Labs for their mesh generation code *classy_blocks*, available at https://github.com/damogranlabs/classy_blocks. Petros Ampatzidis is funded by the Engineering and Physical Sciences Research Council (EPSRC), United Kingdom "Decarbonisation of the Built Environment" CDT grant number EP/L016869/1.

Appendix. Building array validation

This section presents the validation in an urban-like configuration against the experimental dataset of the benchmark case C reported by *AIJ2016*. It comprises a 3×3 building array with cubic buildings with a height of $H = 0.2$ m, placed on a flat ground and impacted by constant airflow. The roughness of the ground is $z_0 = 0.00045$ m (Liu et al., 2019) and the reference mean velocity at building height is $U_0 = 3.654$ m/s, leading to a Reynolds number of $Re = 52{,}000$.

The domain size is $25H \times 35H \times 6H$ and is discretised with $146 \times 220 \times 30$ cells in the streamwise (x), spanwise (y) and vertical (z) dimension, respectively. The dimensions of the computational domain follow the guidelines by Franke et al. (2007). Interpolated profiles for U and TKE are imposed at the inlet based on the wind tunnel measurements. The inlet profile of ε was estimated by assuming that $P_k = \varepsilon$.

The velocity obtained from the present simulations is compared against the experimental measurements by *AIJ2016* and the RANS simulations by Mirzaei and Carmeliet (2013) and Zhang et al. (2018). The former uses the RNG model, while the latter employs the standard $k-\varepsilon$ model; both studies were conducted with ANSYS Fluent and employ a cylindrical computational domain to better model wind's dynamical behaviour. The velocity is made non-dimensional by means of $U_{Ref} = 2.434$ m/s, which is the near-ground inlet velocity at $z/H = 0.1$. Following Tominaga et al. (2004), the simulated velocity is computed as $|U| = \sqrt{\langle u_i \rangle \langle u_i \rangle + 2k}$, where the TKE is used to correct the averaged velocity magnitude taking into account the turbulent contributions.

Fig. A.18 shows the dimensionless velocity magnitude along four selected lines that are the axes of the streets around the central building at height $z/H = 0.1$. The reader is referred to the original experiment for the location of the measurement points, whilst the sampling lines are depicted in Fig. 5c in the main text. Along the streamwise directions (lines $x/H = -1, 1$), the three turbulence models predict similar velocity profiles that reproduce the general features of the motion: a decrease of velocity in the behind-building areas ($|y/H| < 0.5$), and a increase in the street area ($|y/H| > 0.5$). In general, present simulations slightly underestimate the experimental values and literature simulations, which tend to overestimate the experimental velocity, with better agreement achieved in the upwind areas ($x/H = -1$). Some discrepancies between the turbulence models arise in the street area, where the Realizable model better predicts the speed peak at $0.75 \leq |y/H| \leq 1.25$. Along the spanwise directions (lines $y/H = -1, 1$), the RNG and $k-\varepsilon$ models reproduce lower velocity values in the crossroads areas $|x/H| > 0.5$, while the Realizable model exhibits values closer to the experimental measurements.

It is noteworthy to mention the possible presence of errors in experimental measurements and simulations profiles reported in literature: because of the symmetry of the geometry, velocity profiles are expected to be symmetric in x and y direction with respect to the origin. Nonetheless, the experimental data are not symmetric, something that previous studies have not mentioned; this can be possibly due to a short time-average period of the measurements. Also, the literature simulations are not symmetric, and this can be the consequence of a not fully developed RANS simulation.

Fig. A.19 displays the linear regression, the coefficient of determination R^2, the hit rate q, $FAC2$, $NMSE$ and FB metrics (see Section 2.6) for dimensionless velocity magnitude, computed for experiment and simulations in the total number of measurement points available. Similarly to the single building case and previous analyses, all turbulence models perform similarly (R^2 values are almost equivalent), underestimate velocities in the low-velocity regions ($|U|/U_{Ref} < 0.6$) and perform well in the high-velocity regions ($|U|/U_{Ref} > 0.8$). The hit rates of all models are similar ($q = 0.77-0.78$) and within the threshold bounds ($q > 0.66$). The $FAC2$ is close to unity for all the considered turbulence models, the $NMSE$ is close to zero and the FB lies below the threshold value ($|FB| < 0.3$) for all models, suggesting a good overall reproduction of the system airflow velocity.

In general, the present simulations are able to reproduce the main features of the flow, whilst they tend to slightly underestimate the velocity magnitude. The validation is satisfactory, considering also the possible error bars in the experimental data, which have not been reported and are suggested by the lack of symmetry in the profiles.

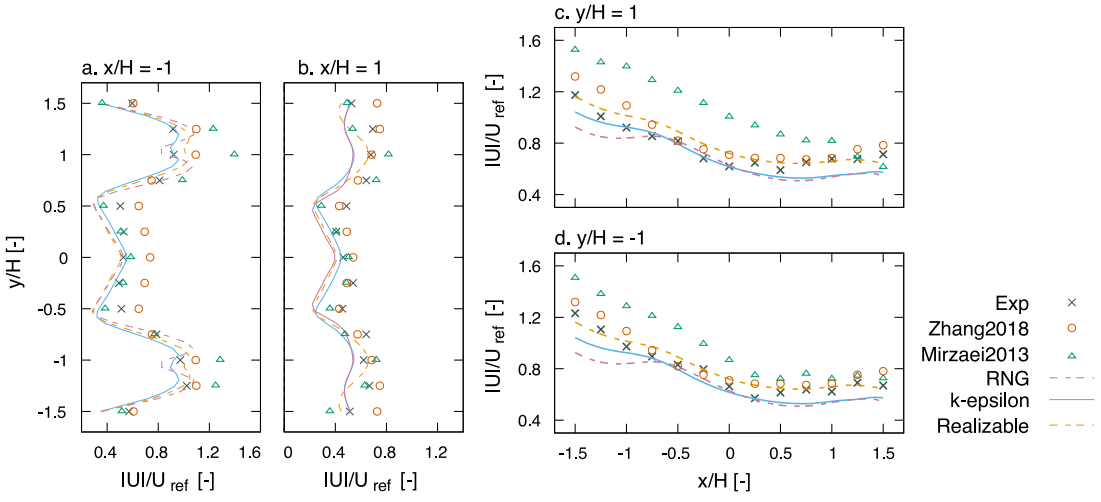

Fig. A.18. Normalised velocity magnitude $|U|$ at the four horizontal lines near the ground at height $z/H = 0.1$. (a) line $x/H = -1$, spanwise direction before the central building; (b) line $x/H = 1$, spanwise direction after the central building; (c) line $y/H = 1$, streamwise direction right-hand side; (d) line $y/h = -1$, streamwise direction left-hand side.

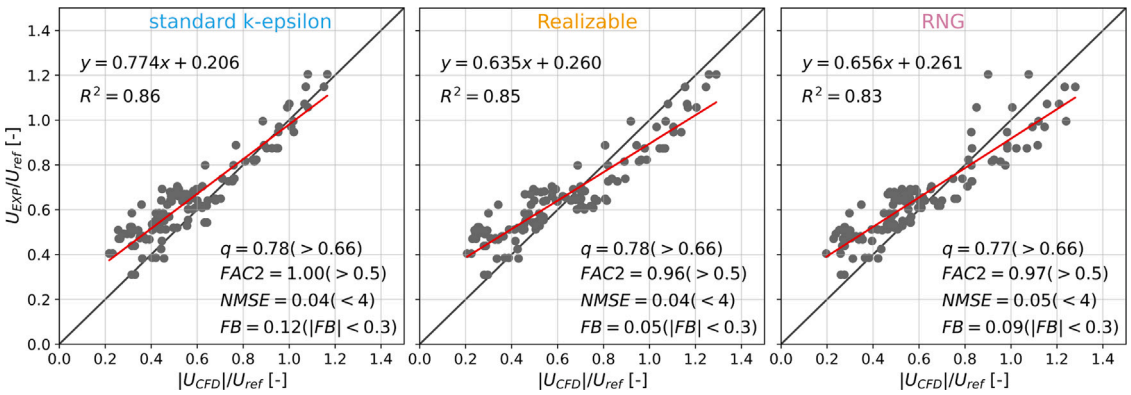

Fig. A.19. Dimensionless velocity magnitude linear regression, coefficient of determination R^2, and validation metrics (q, $FAC2$, $NMSE$ and FB) for the building array case. Comparison between experimental and simulations performed using $k-\varepsilon$, Realizable and RNG turbulence models.

References

Abhijith, K., Kumar, P., Gallagher, J., McNabola, A., Baldauf, R., Pilla, F., Broderick, B., Di Sabatino, S., Pulvirenti, B., 2017. Air pollution abatement performances of green infrastructure in open road and built-up street canyon environments – A review. Atmos. Environ. 162, 71–86.

Aliabadi, A.A., Moradi, M., Clement, D., Lubitz, W.D., Gharabaghi, B., 2019. Flow and temperature dynamics in an urban canyon under a comprehensive set of wind directions, wind speeds, and thermal stability conditions. Environ. Fluid Mech. 19 (1), 81–109.

Allegrini, J., Dorer, V., Carmeliet, J., 2013. Wind tunnel measurements of buoyant flows in street canyons. Build. Environ. 59, 315–326.

Allegrini, J., Dorer, V., Defraeye, T., Carmeliet, J., 2012. An adaptive temperature wall function for mixed convective flows at exterior surfaces of buildings in street canyons. Build. Environ. 49, 55–66.

Ampatzidis, P., Kershaw, T., 2020. A review of the impact of blue space on the urban microclimate. Sci. Total Environ. 730, 139068.

Architectural Institute of Japan, 2016. AIJ Benchmarks for Validation of CFD Simulations Applied to Pedestrian Wind Environment around Buildings. Technical Report, Architectural Institute of Japan.

Arias, P.A., Bellouin, N., Coppola, E., et al., 2021. In: Masson-Delmotte, V., Zhai, P., Pirani, A., Connors, S.L., Péan, C., Berger, S., Caud, N., Chen, Y., Goldfarb, L., Gomis, M.I., Huang, M., Leitzell, K., Lonnoy, E., Matthews, J.B.R., Maycock, T.K., Waterfield, T., Yelekçi, O., Yu, R., Zhou, B. (Eds.), Technical Summary. In: Climate Change 2021: The Physical Science Basis. Contribution of Working Group I to the Sixth Assessment Report of the Intergovernmental Panel on Climate Change. Technical Report, Cambridge University Press, Intergovernmental Panel on Climate Change (IPCC), (in press).

Arnfield, A.J., 2003. Two decades of urban climate research: a review of turbulence, exchanges of energy and water, and the urban heat island. Int. J. Climatol. 23 (1), 1–26.

Baik, J.-J., Kim, J.-J., 2002. On the escape of pollutants from urban street canyons. Atmos. Environ. 36 (3), 527–536, Seventh Internatioonal Conference on Atmospheric Science and Appl ications to Air Quality (ASAAQ).

Bartesaghi Koc, C., Osmond, P., Peters, A., 2018. Evaluating the cooling effects of green infrastructure: A systematic review of methods, indicators and data sources. Sol. Energy 166, 486–508.

Blocken, B., 2014. 50 Years of computational wind engineering: Past, present and future. J. Wind Eng. Ind. Aerodyn. 129, 69–102.

Blocken, B., 2015. Computational fluid dynamics for urban physics: importance, scales, possibilities, limitations and ten tips and tricks towards accurate and reliable simulations. Build. Environ. 91, 219–245, Fifty Year Anniversary for Building and Environment.

Blocken, B., Stathopoulos, T., Carmeliet, J., 2007. CFD simulation of the atmospheric boundary layer: wall function problems. Atmos. Environ. 41 (2), 238–252.

Buccolieri, R., Salizzoni, P., Soulhac, L., Garbero, V., Di Sabatino, S., 2015. The breathability of compact cities. Urban Clim. 13, 73–93.

Celik, I.B., Ghia, U., Roache, P.J., Freitas, C.J., Coleman, H., Raad, P.E., 2008. Procedure for estimation and reporting of uncertainty due to discretization in CFD applications. J. Fluids Eng. 130 (7), 078001.

Çengel, Y.A., Ghajar, A.J., 2015. Heat and Mass Transfer: Fundamentals & Applications. Fifth Edition in SI Units. McGraw-Hill Education, pp. 877–882.

Chen, G., Rong, L., Zhang, G., 2020. Comparison of urban airflow between solar-induced thermal wall and uniform wall temperature boundary conditions by coupling CitySim and CFD. Build. Environ. 172, 106732.

Chew, L.W., Aliabadi, A.A., Norford, L.K., 2018. Flows across high aspect ratio street canyons: Reynolds number independence revisited. Environ. Fluid Mech. 18, 1275–1291.

Cintolesi, C., 2016. Large-Eddy Simulations of Conjugate Heat Transfer with Evaporation-Condensation and Thermal Radiation (Ph.D. thesis). School of Environmental and Industrial Fluid Mechanics, University of Trieste.

Cintolesi, C., Petronio, A., Armenio, V., 2016. Large-eddy simulation of thin film evaporation and condensation from a hot plate in enclosure: First order statistics. Int. J. Heat Mass Transfer 101, 1123–1137.

Cintolesi, C., Petronio, A., Armenio, V., 2017. Large-eddy simulation of thin film evaporation and condensation from a hot plate in enclosure: Second order statistics. Int. J. Heat Mass Transfer 115, 410–423.

Cintolesi, C., Pulvirenti, B., Di Sabatino, S., 2021. Large-eddy simulations of pollutant removal enhancement from urban canyons. Bound.-Lay. Meteorol. 180 (79), 104.

Coceal, O., Thomas, T.G., Castro, I.P., Belcher, S.E., 2006. Mean flow and turbulence statistics over groups of urban-like cubical obstacles. Bound.-Lay. Meteorol. 121 (3), 491–519.

Di Sabatino, S., Barbano, F., Brattich, E., Pulvirenti, B., 2020. The multiple-scale nature of urban heat island and its footprint on air quality in real urban environment. Atmosphere 11 (11).

Di Sabatino, S., Buccolieri, R., Salizzoni, P., 2013. Recent advancements in numerical modelling of flow and dispersion in urban areas: a short review. Int. J. Environ. Pollut. 52 (3–4), 172–191.

EC, 2015. Towards an EU Research and Innovation Policy Agenda for Nature-Based Solutions & Re-Naturing Cities : Final Report of the Horizon 2020 Expert Group on 'Nature-Based Solutions and Re-Naturing Cities'. Publications Office, European Commission and Directorate-General for Research and Innovation.

ESI-OpenCFD, 2006. OpenFOAM®, OpenCFD Ltd Release version 2006. web: https://www.openfoam.com/news/main-news/openfoam-v20-06. (Accessed 03 2022).

Fernando, H.J.S., Zajic, D., Di Sabatino, S., Dimitrova, R., Hedquist, B., Dallman, A., 2010. Flow, turbulence, and pollutant dispersion in urban atmospheres. Phys. Fluids 22 (5), 051301.

Ferziger, J.H., Perić, M., 2002. Computational Methods for Fluid Dynamics, 3rd rev. ed. Springer Science & Business Media.

Franke, J., Hellsten, A., Schlünzen, H., Carissimo, B., 2007. Best practice guideline for the CFD simulation of flows in the urban environment. In: COST Action 732.

Gallotti, G., Santo, M.A., Apostolidou, I., Alessandri, J., Armigliato, A., Basu, B., Debele, S., Domeneghetti, A., Gonzalez-Ollauri, A., Kumar, P., Mentzafou, A., Pilla, F., Pulvirenti, B., Ruggieri, P., Sahani, J., Salmivaara, A., Basu, A.S., Spyrou, C., Pinardi, N., Toth, E., Unguendoli, S., Pillai, U.P.A., Valentini, A., Varlas, G., Verri, G., Zaniboni, F., Di Sabatino, S., 2021. On the management of nature-based solutions in open-air laboratories: New insights and future perspectives. Resources 10 (4).

Gousseau, P., Blocken, B., van Heijst, G.J.F., 2013. Quality assessment of Large-Eddy Simulation of wind flow around a high-rise building: Validation and solution verification. Comput. & Fluids 79, 120–133.

Gunawardena, K., Wells, M., Kershaw, T., 2017. Utilising green and bluespace to mitigate urban heat island intensity. Sci. Total Environ. 584–585, 1040–1055.

Hargreaves, D., Wright, N., 2007. On the use of the k–ε model in commercial CFD software to model the neutral atmospheric boundary layer. J. Wind Eng. Ind. Aerodyn. 95 (5), 355–369.

Heusinkveld, B.G., Steeneveld, G.J., van Hove, L.W.A., Jacobs, C.M.J., Holtslag, A.A.M., 2014. Spatial variability of the Rotterdam urban heat island as influenced by urban land use. J. Geophys. Res.: Atmos. 119 (2), 677–692.

Huang, L., Li, J., Zhao, D., Zhu, J., 2008. A fieldwork study on the diurnal changes of urban microclimate in four types of ground cover and urban heat island of Nanjing, China. Build. Environ. 43 (1), 7–17.

Ibrahim, Y., Kershaw, T., Shepherd, P., Elwy, I., 2021. A parametric optimisation study of urban geometry design to assess outdoor thermal comfort. Sustainable Cities Soc. 75, 103352.

Imam Syafii, N., Ichinose, M., Kumakura, E., Jusuf, S.K., Chigusa, K., Wong, N.H., 2017. Thermal environment assessment around bodies of water in urban canyons: A scale model study. Sustainable Cities Soc. 34, 79–89.

IPCC, 2021. Summary for Policymakers. In: Climate Change 2021: The Physical Science Basis. Contribution of Working Group I to the Sixth Assessment Report of the Intergovernmental Panel on Climate Change. Technical Report, Cambridge University Press, Intergovernmental Panel on Climate Change (IPCC), (in press).

Ishii, A., Iwamoto, S., Katayama, T., Hayashi, T., Shiotsuki, Y., Kitayama, H., Tsutsumi, J.-I., Nishida, M., 1991. A comparison of field surveys on the thermal environment in urban areas surroundings a large pond: when filled and when drained. Energy Build. 16 (3), 965–971.

Jacobs, C., Klok, L., Bruse, M., Cortesão, J.a., Lenzholzer, S., Kluck, J., 2020. Are urban water bodies really cooling? Urban Clim. 32, 100607.

Kabisch, N., Frantzeskaki, N., Pauleit, S., Naumann, S., Davis, M., Artmann, M., Haase, D., Knapp, S., Korn, H., Stadler, J., Zaunberger, K., Bonn, A., 2016. Nature-based solutions to climate change mitigation and adaptation in urban areas: perspectives on indicators, knowledge gaps, barriers, and opportunities for action. Ecol. Soc. 21 (2).

Kanda, M., Kanega, M., Kawai, T., Moriwaki, R., Sugawara, H., 2007. Roughness lengths for momentum and heat derived from outdoor urban scale models. J. Appl. Meteorol. Climatol. 46 (7), 1067–1079.

Kanda, I., Yamao, Y., 2016. Passive scalar diffusion in and above urban-like roughness under weakly stable and unstable thermal stratification conditions. J. Wind Eng. Ind. Aerodyn. 148, 18–33.

Kato, T., Nakane, K., Yamada, T., 2009. Fundamental experiment of evaporation mechanism on small scale water surface. In: Proceedings of Hydraulic Engineering, Japan Society of Civil Engineers. Vol. 53. pp. 343–348 (in Japanese).

Kim, J.-J., Baik, J.-J., 1999. A numerical study of thermal effects on flow and pollutant dispersion in urban street canyons. J. Appl. Meteorol. 38 (9), 1249–1261.

Kim, J.-J., Baik, J.-J., 2005. Physical experiments to investigate the effects of street bottom heating and inflow turbulence on urban street-canyon flow. Adv. Atmos. Sci. 22 (2), 230–237.

Klok, L., Rood, N., Kluck, J., Kleerekoper, L., 2019. Assessment of thermally comfortable urban spaces in Amsterdam during hot summer days. Int. J. Biometeorol. 63 (2), 129–141.

Kovar-Panskus, A., Moulinneuf, L., Savory, E., et al., 2002. A wind tunnel investigation of the influence of solar-induced wall-heating on the flow regime within a simulated urban street canyon. Water Air Soil Pollut. Focus 2, 555–571.

Launder, B.E., Spalding, D.B., 1974. The numerical computation of turbulent flows. Comput. Methods Appl. Mech. Engrg. 3 (2), 269–289.

Liu, C., Kershaw, T., Fosas, D., Ramallo Gonzalez, A., Natarajan, S., Coley, D., 2017. High resolution mapping of overheating and mortality risk. Build. Environ. 122, 1–14.

Liu, J., Zhang, X., Niu, J., Tse, K.T., 2019. Pedestrian-level wind and gust around buildings with a 'lift-up' design: Assessment of influence from surrounding buildings by adopting LES. Build. Simul. 12 (6), 1107–1118.

Marucci, D., Carpentieri, M., 2020. Stable and convective boundary-layer flows in an urban array. J. Wind Eng. Ind. Aerodyn. 200, 104140.

McMullan, W., Angelino, M., 2022. The effect of tree planting on traffic pollutant dispersion in an urban street canyon using large eddy simulation with a recycling and rescaling inflow generation method. J. Wind Eng. Ind. Aerodyn. 221, 104877.

Meng, Y., Hibi, K., 1998. Turbulent measurments of the flow field around a high-rise building. Wind Eng. JAWE 1998 (76), 55–64 (in Japanese).

Mirzaei, P.A., Carmeliet, J., 2013. Dynamical computational fluid dynamics modeling of the stochastic wind for application of urban studies. Build. Environ. 70, 161–170.

Mochida, A., Tominaga, Y., Murakami, S., Yoshie, R., Ishihara, T., Ooka, R., 2002. Comparison of various $k-\varepsilon$ models and DSM applied to flow around a high-rise building – report on AIJ cooperative project for CFD prediction of wind environment –. Wind Struct. 5 (2_3_4), 227–244.

Moonen, P., Defraeye, T., Dorer, V., Blocken, B., Carmeliet, J., 2012. Urban physics: Effect of the micro-climate on comfort, health and energy demand. Front. Archit. Res. 1 (3), 197–228.

Oke, T.R., Mills, G., Christen, A., Voogt, J.A., 2017. Urban Climates. Cambridge University Press.

Patankar, S.V., 1980. Numerical Heat Transfer and Fluid Flow, first ed. CRC Press, Boca Raton, USA, p. 214.

Patankar, S.V., Spalding, D.B., 1972. A calculation procedure for heat, mass and momentum transfer in three-dimensional parabolic flows. Int. J. Heat Mass Transfer 15 (10), 1787–1806.

Pauken, M.T., 1998. An experimental investigation of combined turbulent free and forced evaporation. Exp. Therm Fluid Sci. 18 (4), 334–340.

Petronio, A., 2010. Numerical Investigation of Condensation and Evaporation Effects Inside a Tub (Ph.D. thesis). School of Environmental and Industrial Fluid Mechanics, University of Trieste.

Pope, S.B., 2013. Turbulent Flows. Taylor & Francis, London.

Princevac, M., Baik, J.-J., Li, X., Pan, H., Park, S.-B., 2010. Lateral channeling within rectangular arrays of cubical obstacles. J. Wind Eng. Ind. Aerodyn. 98 (8), 377–385.

Ramponi, R., Blocken, B., de Coo, L.B., Janssen, W.D., 2015. CFD simulation of outdoor ventilation of generic urban configurations with different urban densities and equal and unequal street widths. Build. Environ. 92, 152–166.

Ricci, A., Blocken, B., 2020. On the reliability of the 3D steady RANS approach in predicting microscale wind conditions in seaport areas: The case of the ijmuiden sea lock. J. Wind Eng. Ind. Aerodyn. 207, 104437.

Richards, P.J., Hoxey, R.P., 1993. Appropriate boundary conditions for computational wind engineering models using the k-ε turbulence model. J. Wind Eng. Ind. Aerodyn. 46–47, 145–153, Proceedings of the 1st International on Computational Wind Engineering.

Richards, P., Norris, S., 2011. Appropriate boundary conditions for computational wind engineering models revisited. J. Wind Eng. Ind. Aerodyn. 99 (4), 257–266, The Fifth International Symposium on Computational Wind Engineering.

Roache, P.J., 1994. Perspective: A method for uniform reporting of grid refinement studies. J. Fluids Eng. Trans. ASME 116 (3).

Roache, P.J., 1997. Quantification of uncertainty in computational fluid dynamics. Annu. Rev. Fluid Mech. 29 (1), 123–160.

Ruangpan, L., Vojinovic, Z., Di Sabatino, S., Leo, L.S., Capobianco, V., Oen, A.M.P., McClain, M.E., Lopez-Gunn, E., 2020. Nature-based solutions for hydro-meteorological risk reduction: a state-of-the-art review of the research area. Nat. Hazards Earth Syst. Sci. 20 (1), 243–270.

Saaroni, H., Ziv, B., 2003. The impact of a small lake on heat stress in a Mediterranean urban park: the case of Tel Aviv, Israel. Int. J. Biometeorol. 47 (3), 156–165.

Santamouris, M., 2015. Analyzing the heat island magnitude and characteristics in one hundred Asian and Australian cities and regions. Sci. Total Environ. 512–513, 582–598.

Santamouris, M., Osmond, P., 2020. Increasing green infrastructure in cities: Impact on ambient temperature, air quality and heat-related mortality and morbidity. Buildings 10 (12), 233.

Schatzmann, M., Olesen, H., Franke, J., 2010. COST 732 Model Evaluation Case Studies: Approach and Results. COST Action 732 Technical Report, COST Office.

Seddon, N., Chausson, A., Berry, P., Girardin, C.A.J., Smith, A., Turner, B., 2020. Understanding the value and limits of nature-based solutions to climate change and other global challenges. Philos. Trans. R. Soc. B 375 (1794), 20190120.

Shih, T.-H., Liou, W.W., Shabbir, A., Yang, Z., Zhu, J., 1995. A new k-ε eddy viscosity model for high reynolds number turbulent flows. Comput. & Fluids 24 (3), 227–238.

Shirzadi, M., Mirzaei, P.A., Naghashzadegan, M., 2017. Improvement of k-epsilon turbulence model for CFD simulation of atmospheric boundary layer around a high-rise building using stochastic optimization and Monte Carlo sampling technique. J. Wind Eng. Ind. Aerodyn. 171, 366–379.

Sosnowski, P., 2013. Numerical Investigation of Evaporation and Condensation of Thin Films in Conjugated Heat Transfer Systems (Ph.D. thesis). School of Environmental and Industrial Fluid Mechanics, University of Trieste.

Sosnowski, P., Petronio, A., Armenio, V., 2013. Numerical model for thin liquid film with evaporation and condensation on solid surfaces in systems with conjugated heat transfer. Int. J. Heat Mass Transfer 66, 382–395.

Steeneveld, G.J., Koopmans, S., Heusinkveld, B.G., Theeuwes, N.E., 2014. Refreshing the role of open water surfaces on mitigating the maximum urban heat island effect. Landsc. Urban Plan. 121, 92–96.

Sun, R., Chen, L., 2012. How can urban water bodies be designed for climate adaptation? Landsc. Urban Plan. 105 (1), 27–33.

Sweby, P.K., 1984. High resolution schemes using flux limiters for hyperbolic conservation laws. SIAM J. Numer. Anal. 21, 995–1011.

Theeuwes, N.E., Solcerová, A., Steeneveld, G.J., 2013. Modeling the influence of open water surfaces on the summertime temperature and thermal comfort in the city. J. Geophys. Res.: Atmos. 118 (16), 8881–8896.

Toja-Silva, F., Kono, T., Peralta, C., Lopez-Garcia, O., Chen, J., 2018. A review of computational fluid dynamics CFD simulations of the wind flow around buildings for urban wind energy exploitation. J. Wind Eng. Ind. Aerodyn. 180, 66–87.

Toja-Silva, F., Peralta, C., Lopez-Garcia, O., Navarro, J., Cruz, I., 2015. Roof region dependent wind potential assessment with different RANS turbulence models. J. Wind Eng. Ind. Aerodyn. 142, 258–271.

Tominaga, Y., 2015. Flow around a high-rise building using steady and unsteady RANS CFD: Effect of large-scale fluctuations on the velocity statistics. J. Wind Eng. Ind. Aerodyn. 142, 93–103.

Tominaga, Y., Mochida, A., Shirasawa, T., Yoshie, R., Kataoka, H., Harimoto, K., Nozu, T., 2004. Cross comparisons of CFD results of wind environment at pedestrian level around a high-rise building and within a building complex. J. Asian Archit. Build. Eng. 3 (1), 63–70.

Tominaga, Y., Mochida, A., Yoshie, R., Kataoka, H., Nozu, T., Yoshikawa, M., Shirasawa, T., 2008. AIJ guidelines for practical applications of CFD to pedestrian wind environment around buildings. J. Wind Eng. Ind. Aerodyn. 96 (10), 1749–1761, 4th International Symposium on Computational Wind Engineering (CWE2006).

Tominaga, Y., Sato, Y., Sadohara, S., 2015. CFD simulations of the effect of evaporative cooling from water bodies in a micro-scale urban environment: Validation and application studies. Sustainable Cities Soc. 19, 259–270.

Trindade da Silva, F., Reis, N.C., Santos, J.M., Goulart, E.V., Engel de Alvarez, C., 2021. The impact of urban block typology on pollutant dispersion. J. Wind Eng. Ind. Aerodyn. 210, 104524.

Tsalicoglou, C., Allegrini, J., Carmeliet, J., 2020. Non-isothermal flow between heated building models. J. Wind Eng. Ind. Aerodyn. 204, 104248.

Vardoulakis, S., Fisher, B.E.A., Pericleous, K., Gonzalez-Flesca, N., 2003. Modelling air quality in street canyons: a review. Atmos. Environ. 37 (2), 155–182.

Welty, J., Wicks, C., Rorrer, G., Wilson, R., 2007. Fundamentals of Momentum, Heat and Mass Transfer. Wiley.

Xue, Z., Hou, G., Zhang, Z., Lyu, X., Jiang, M., Zou, Y., Shen, X., Wang, J., Liu, X., 2019. Quantifying the cooling-effects of urban and peri-urban wetlands using remote sensing data: Case study of cities of northeast China. Landsc. Urban Plan. 182, 92–100.

Yakhot, V., Orszag, S.A., 1986. Renormalization group analysis of turbulence. I. Basic theory. J. Sci. Comput. 1 (1), 3–51.

Yoshie, R., Mochida, A., Tominaga, Y., Kataoka, H., Harimoto, K., Nozu, T., Shirasawa, T., 2007. Cooperative project for CFD prediction of pedestrian wind environment in the Architectural Institute of Japan. J. Wind Eng. Ind. Aerodyn. 95 (9), 1551–1578.

Yu, Z., Yang, G., Zuo, S., Jørgensen, G., Koga, M., Vejre, H., 2020. Critical review on the cooling effect of urban blue-green space: A threshold-size perspective. Urban Forestry Urban Green. 49, 126630.

Zhang, R., Mirzaei, P.A., Jones, B., 2018. Development of a dynamic external CFD and BES coupling framework for application of urban neighbourhoods energy modelling. Build. Environ. 146, 37–49.

Zhao, Y., Chew, L.W., c Kubilay, A., Carmeliet, J., 2020. Isothermal and non-isothermal flow in street canyons: A review from theoretical, experimental and numerical perspectives. Build. Environ. 184, 107163.

Žuvela-Aloise, M., Koch, R., Buchholz, S., Früh, B., 2016. Modelling the potential of green and blue infrastructure to reduce urban heat load in the city of Vienna. Clim. Change 135 (3–4), 425–438.